LBL-20324

Search for Right-Handed Currents by Means of Muon Spin Rotation

David Philip Stoker

Ph.D. Thesis

Lawrence Berkeley Laboratory
University of California
Berkeley, California 94720

September 1985

Search for Right-Handed Currents by Means of Muon Spin Rotation

David Philip Stoker

Abstract

A muon spin rotation (μSR) technique has been used to place limits on right-handed weak currents in μ^+ decay. A beam of almost 100% polarized 'surface' muons obtained from the TRIUMF M13 beamline was stopped in essentially non-depolarizing >99.99% pure metal foils. The μ^+ spins were precessed by 70-G or 110-G transverse fields. Decay e^+ emitted within 225 mrad of the beam direction and with momenta above 46 MeV/c were momentum-analyzed to 0.2%. Comparison of the μSR signal amplitude with that expected for (V-A) decay yields an endpoint asymmetry $\xi P_\mu \delta/\rho > 0.9951$ with 90% confidence. In the context of manifest left-right symmetric models with massless neutrinos the results imply the 90% confidence limits $M(W_2) > 381$ GeV/c^2 and $-0.057 < \zeta < 0.044$, where W_2 is a predominantly right-handed gauge boson and ζ is the left-right mixing angle. Limits on $M(W_2)$ for $M(\nu_{\mu R}) \neq 0$ are also presented. The endpoint asymmetry is used to deduce limits on the $\nu_{\mu L}$ mass and helicity in π^+ decay, non-(V-A) couplings in helicity projection form, and the mass scale of composite leptons.

Table of Contents

Acknowledgments

This thesis owes much to the efforts of the other collaboration members participating in TRIUMF experiments E185 and E247: Brian Balke, John Carr, George Gidal, Bruno Gobbi, Alex Jodidio, Chris Oram, Kirk Shinsky (deceased), Herb Steiner, Mark Strovink, and Bob Tripp. The technical assistance of C. Covey, R. Fuzesy, F. Goozen, P.Harding, M. Morrison, and P. Robrish at L.B.L. and the support of the TRIUMF staff contributed to the success of the experiments.

I would particularly like to thank my advisor Mark Strovink, who having advised me initially that a thesis could be completed in $2+\varepsilon$ years, continued to provide patient support and advice as ε grew to 2.7.

I would also like to thank Marjorie Olmstead for helpful discussions of relevant aspects of solid state physics.

The assistance of Pat Bronnenberg in typing much of this thesis and other material is greatly appreciated.

The research reported here was supported in part by the U.S. Department of Energy through Contracts No. DE-AC03-76SF00098 and AC02-ER02289.

Chapter 1

Introduction

In the course of more than a decade of remarkable agreement with experiment the Glashow-Weinberg-Salam model[1-3], based on the gauge group $SU(2)_L \times U(1)$, has become accepted as the 'standard model' of electroweak interactions. Despite its outstanding success the standard model does not explain the left-handed character of the charged current weak interactions such as β and μ decay. Instead the left-handedness is built in a priori by allowing only the left-handed components of fermions to couple to the charged gauge bosons. Shortly before Weinberg and Salam unified the weak and electromagnetic interactions, Lipmanov[4] asked

> "...whether the nonconservation of parity in weak interactions is not a manifestation of a violated (V±A) symmetry of these interactions, with (V-A) dominance... It is possible that the coupling between the weak interaction currents is mediated by intermediate vector bosons. Then one can imagine that there exist intermediate bosons of two kinds, $W^{(V-A)}$ and $W^{(V+A)}$, which mediate the (V-A) and (V+A) couplings, respectively. If the mass of the $W^{(V-A)}$ and $W^{(V+A)}$ were equal, there would be no experimental manifestation of parity non-conservation. However, the latter effect appears if there is a mass difference for the two intermediate bosons. The effective current-current Lagrangian for the weak interactions... has the form (for $q^2 << M^2$):

$$L_W = (G/\sqrt{2}) J^{(V-A)} J^{(V-A)*} + (G_1/\sqrt{2}) J^{(V+A)} J^{(V+A)*}$$

where $G/\sqrt{2} = 4\pi g^2/M^2_{(V-A)}$, $G_1/\sqrt{2} = 4\pi g^2/M^2_{(V+A)}$ "

Lipmanov went on to show that the electron emission asymmetry in muon decay provided an estimate $G_1 \leq 0.12G$, and that the μ^+ from π^+ decay would be partially depolarized, with longitudinal polarization $P_\mu = 1-2G_1^2/G^2$.

The more recent left-right symmetric theories[5,6], in which the standard electroweak gauge group is extended to $SU(2)_L \times SU(2)_R \times U(1)$, embody the spirit of the Lipmanov formulation. Although completely left-right symmetric at the Lagrangian level these theories admit asymmetric solutions through spontaneous symmetry breaking which violate parity[7]. In particular, the Higgs mechanism can impart a larger mass to W_R than to W_L, thereby suppressing the right-handed currents at low q^2 while retaining parity conservation for $q^2 >> M^2(W_R)$.

This thesis presents the results of a search for deviations from the (V-A) prediction for the e^+ asymmetry in polarized μ^+ decay at rest by means of a muon spin rotation (μSR) technique. The recent development[8] of 'surface' beams has provided muon beams with essentially the polarization intrinsic to pion decay at rest. Naturally, right-handed currents may contribute at each step of the $\pi \to \mu \to e$ decay chain thus enhancing the experimental sensitivity.

The experiment was operated in two modes, each sensitive to right-handed currents but with different major sources of possible systematic error. In each case the μ^+ beam was stopped in metal targets. In metals, unlike many other materials, the μ^+ are thermalized in a quasi-free state instead of as muonium (μ^+e^-) where hyperfine transitions rapidly reduce the muon polarization by 50%. In the first

mode[9]) the spins of the stopped μ^+ were held in a 1.1-T field which quenches muon depolarization in any residual muonium through the Paschen-Back effect. Measurement of the momentum spectrum endpoint decay rate opposite to the μ^+ spin, which vanishes for a purely (V-A) interaction, allows limits to be set on any right-handed current admixture. In the second mode, which provided the data presented here, the μ^+ spins were instead precessed by 70-G or 110-G fields transverse to the beam direction. The time variation of the e^+ emission rate near the beam direction as the μ^+ spins precess constitute the μSR signal. Limits on right-handed currents are set by comparing the μSR signal amplitude with that expected for a (V-A) interaction.

The experiment was conceived in mid-1980 and most of the apparatus was constructed during 1981. The data presented in this thesis was accumulated during the three running periods of experiments E185 and E247 at the TRIUMF cyclotron during 1982-4.

Chapter 2

The Standard and Left-Right Symmetric Models

2.1 The Standard Model: A Brief Review

The gauge group of the standard electroweak model is $SU(2)_L \times U(1)_Y$ with coupling constants g and g' respectively. The leptons and quark weak eigenstates are assigned to left-handed SU(2) doublets

$$\begin{bmatrix}\nu_e \\ e^-\end{bmatrix}_L, \begin{bmatrix}\nu_\mu \\ \mu^-\end{bmatrix}_L, \ldots \qquad \begin{bmatrix}u \\ d'\end{bmatrix}_L, \begin{bmatrix}c \\ s'\end{bmatrix}_L, \ldots$$

and right-handed singlets.

The simplest Higgs assignment required to break down the symmetry to $U(1)_{em}$, thereby guaranteeing the masslessness of the photon, is the scalar $SU(2)_L$ doublet

$$\Phi = \begin{bmatrix}\phi^+ \\ \phi^o\end{bmatrix}$$

Minimizing the Higgs potential yields a non-zero vacuum expectation value solution

$$\Phi = \begin{bmatrix}0 \\ v\end{bmatrix}$$

which imparts masses to the W and Z bosons and the fermions. With the Weinberg angle θ_W defined by $\tan\theta_W = g'/g$ the gauge fields $\vec{W}=(W^1,W^2,W^3)$ and B, associated with $SU(2)_L$ and $U(1)_Y$ respectively, become the physical boson eigenstates

$$W^\pm = (W^1 \mp iW^2)/\sqrt{2} \qquad M_W^2 = g^2v^2/2$$

$$Z = W^3\cos\theta_W - B\sin\theta_W \qquad M_Z^2 = (g^2+g'^2)v^2/2$$

$$Y = W^3\sin\theta_W + B\cos\theta_W \qquad M_\gamma = 0$$

Comparison of single W exchange in the low-energy limit with the corresponding four-fermion contact interaction gives $g^2/8M_W^2 = G_F/\sqrt{2}$ where G_F is the Fermi coupling constant. In addition, the form of the electromagnetic current allows the electronic charge $e = \sqrt{(4\pi\alpha)}$ to be related to g and g' by $e = g\sin\theta_W = g'\cos\theta_W$. Then to lowest order and ignoring radiative corrections the standard model predicts

$$M_W = \frac{1}{\sin\theta_W}\left[\frac{\pi\alpha}{G_F\sqrt{2}}\right]^{1/2} = \frac{37.3}{\sin\theta_W}\ \text{GeV}$$

and

$$M_Z = \frac{M_W}{\cos\theta_W} = \frac{74.6}{\cos 2\theta_W}\ \text{GeV}$$

Table (2.1) shows the experimental masses from the UA-1[10] and UA-2[11] collaborations at CERN together with the standard model predictions of Marciano and Sirlin[12]. The theoretical predictions use $\sin^2\theta_W$=0.217±0.014 obtained from deep inelastic ν_μ scattering and the e-D scattering asymmetry after applying radiative corrections.

	UA-1	UA-2	Standard Model
M_W (GeV)	80.9±1.5±2.4	81.0±2.5±1.3	$83.0^{+2.9}_{-2.7}$
M_Z (GeV)	95.6±1.5±2.9	91.9±1.3±1.4	$93.8^{+2.4}_{-2.2}$

Table (2.1)

The minimal standard model has one as yet unobserved physical

neutral scalar Higgs with a mass M_H not predicted by the theory. However, stability of the physical vacuum requires $M_H > 7$ GeV and the weak interactions are predicted to become strong at high energies unless $M_H < 1$ TeV.

2.2 Left-Right Symmetric Model: An Introduction

The gauge group of left-right symmetric models is $SU(2)_L \times SU(2)_R \times U(1)_{B-L}$ with coupling constants g_L, g_R, and g' respectively. Only manifest left-right symmetric models, for which $g_L = g_R = g$, are considered here. Compared to the standard model, the left-right symmetric model requires an extra set of gauge bosons and a more complex Higgs structure to produce the fermion and gauge boson masses. The left- and right-handed fermion components are assigned to isospin doublets $\psi_{L,R}$ with the indicated quantum numbers $(T_L, T_R, B\text{-}L)$:

$$\begin{bmatrix}\nu_e\\ e^-\end{bmatrix}_L, \begin{bmatrix}\nu_\mu\\ \mu^-\end{bmatrix}_L, \ldots \qquad \begin{bmatrix}\nu_e\\ e^-\end{bmatrix}_R, \begin{bmatrix}\nu_\mu\\ \mu^-\end{bmatrix}_R, \ldots \qquad \begin{bmatrix}u\\ d'\end{bmatrix}_L, \begin{bmatrix}c\\ s'\end{bmatrix}_L, \ldots \qquad \begin{bmatrix}u\\ d'\end{bmatrix}_R, \begin{bmatrix}c\\ s'\end{bmatrix}_R, \ldots$$

$$(1/2,0,-1) \qquad (0,1/2,-1) \qquad (1/2,0,1/3) \qquad (0,1/2,1/3)$$

The generation of Dirac masses, $\propto(\psi_R\psi_L + \psi_L\psi_R)$, for the fermions requires Yukawa couplings to Higgs multiplets with quantum numbers $(1/2,1/2^*,0)$ since the mass terms in the Lagrangian must be Lorentz scalars. The required multiplets of complex scalar fields are

$$\Phi = \begin{bmatrix}\phi_1^0 & \phi_1^+\\ \phi_2^- & \phi_2^0\end{bmatrix} \qquad \tilde{\Phi} = \tau_2\Phi^*\tau_2$$

Additional Higgs multiplets are needed to complete the symmetry breakdown to $U(1)_{em}$. The simplest choice is the doublets

$$X_L = \begin{bmatrix} X_L^+ \\ X_L^o \end{bmatrix} \qquad X_R = \begin{bmatrix} X_R^+ \\ X_R^o \end{bmatrix}$$

with quantum numbers (1/2,0,1) and (0,1/2,1) respectively. Although the classical Higgs potential is symmetric under $X_L \leftrightarrow X_R$, Senjanovic[13] has shown that for a range of coefficients an asymmetric solution

$$\langle X_L \rangle = 0, \qquad \langle X_R \rangle = \begin{bmatrix} 0 \\ v \end{bmatrix}, \qquad \langle \Phi \rangle = \begin{bmatrix} k & 0 \\ 0 & k' \end{bmatrix}$$

emerges as the absolute minimum of the potential.

The gauge fields $\vec{W}_L$, $\vec{W}_R$, and B associated with $SU(2)_L$, $SU(2)_R$, and $U(1)_{B-L}$ respectively, combine to form the mass eigenstates $W_1^{\pm}$, $W_2^{\pm}$, Z_1, Z_2 and γ. In general, the Higgs mechanism which gives masses to the gauge bosons also produces a left-right mixing. The physical charged bosons are

$$\begin{bmatrix} W_1 \\ W_2 \end{bmatrix}^{\pm} = \begin{bmatrix} \cos\zeta & \sin\zeta \\ -\sin\zeta & \cos\zeta \end{bmatrix} \begin{bmatrix} W_L \\ W_R \end{bmatrix}^{\pm}$$

where $W_{L,R}^{\pm} = (W_{L,R}^1 \mp i W_{L,R}^2)/\sqrt{2}$ and $\tan 2\zeta = -4kk'/v^2$. The experimental constraints that ζ is small and $M(W_2) \gg M(W_1)$ [section (2.5)] imply $v \gg k,k'$, and then

$$M^2(W_1) = g^2(k^2+k'^2)/2$$

$$M^2(W_2) = g^2(v^2+k^2+k'^2)/2$$

With θ_W', the analog of the Weinberg angle, defined by $\sin^2\theta_W' = g'^2/(g^2+g'^2)$ the physical neutral bosons are

$$\gamma = (W_L^3 + W_R^3)\sin\theta_W' + B\sqrt{(\cos 2\theta_W')}$$

$$Z_1 = W_L^3\cos\theta_W' - W_R^3\sin\theta_W'\tan\theta_W' - B\tan\theta_W'\sqrt{(\cos 2\theta_W')}$$

$$Z_2 = W_R^3\sqrt{(\cos 2\theta_W')}/\cos\theta_W' - B\tan\theta_W'$$

with masses $M(\gamma) = 0$

$$M(Z_1) = M(W_1)/\cos\theta_W'$$

$$M(Z_2) = M(W_2)\cos\theta_W'/\sqrt{(\cos 2\theta_W')}$$

In addition, for the above choice of Higgs multiplets, there remain six neutral and four charged physical Higgs scalars. In the model of Senjanovic[13] one neutral Higgs has a mass $-(M(W_1))$ and the rest have masses $-(M(W_2))$.

In the limit $M(W_2) \to \infty$ the predictions of the left-right symmetric model are identical to those of the standard model for both the charged and neutral currents. Also, in the limit $\zeta \to 0$ but with $M(W_2)$ finite both models make identical predictions for the parity violating neutral currents.

2.3 Neutrinos: Dirac or Majorana?

The ν_L of the standard electroweak model may be either Dirac or Majorana particles. In the Dirac case ν_L and ν_R are different helicity states of the same particle, and ν_R is assigned to an SU(2) singlet. However, for Majorana neutrinos ν_L and ν_R are different particles, and ν_R is absent from the standard model.

The situation is more complex in the left-right symmetric model where, depending on the choice of Higgs structure, the neutrinos may

acquire both Majorana and Dirac masses. As will be seen below this provides an explanation, first proposed by Gell-Mann, Ramond and Slansky[14], for the smallness of the ν_L mass. It also has a major impact on the observability of right-handed currents in low-energy processes [section (2.4)].

The Dirac and Majorana mass terms have the structures and $(T_L, T_R, B-L)$ quantum numbers:

Dirac:	$(\bar{\nu}_R \nu_L + \bar{\nu}_L \nu_R)$	(1/2,1/2,0)
Majorana:	$(\bar{\nu}^c_L \nu_L + \bar{\nu}_L \nu^c_L)$ and $(\bar{\nu}^c_R \nu_R + \bar{\nu}_R \nu^c_R)$	(1,0,-2) and (0,1,-2)

Only Dirac mass terms, through Yukawa couplings to the multiplet Φ, are possible for the Higgs assignment of section (2.2).

Mohapatra and Senjanovic[15] have proposed a model in which two Majorana neutrinos ν and N are assigned to the lepton doublets

$$\begin{bmatrix} \nu_{eL} \\ e^-_L \end{bmatrix}, \ldots \qquad \begin{bmatrix} N_{eR} \\ e^-_R \end{bmatrix}, \ldots$$

prior to spontaneous symmetry breaking, and the Higgs multiplets $X_{L,R}$ are replaced by $\Delta_L(1,0,2)$ and $\Delta_R(0,1,2)$ which generate the additional Majorana mass terms. The new Higgs structure is somewhat more complicated with

$$\Delta_{L,R} = \begin{bmatrix} \delta^+/\sqrt{2} & \delta^{++} \\ \delta^0 & -\delta^+/\sqrt{2} \end{bmatrix}_{L,R}$$

With an analogous pattern of vacuum expectation values, $\langle \Delta_L \rangle = 0$ and

$\langle\Delta_R^0\rangle = v$, the Majorana mass term for ν_L vanishes while that for N_R is $-M(W_2)$. The off-diagonal Dirac mass terms ($-M_\ell$ for $\ell = e, \mu, \tau$) cause a slight left-right mixing so that the mass eigenstates ν_1 and ν_2 are

$$\begin{bmatrix} \nu_1 \\ \nu_2 \end{bmatrix} = \begin{bmatrix} \cos\delta & \sin\delta \\ -\sin\delta & \cos\delta \end{bmatrix} \begin{bmatrix} \nu_L \\ N_R \end{bmatrix}$$

with masses $$M(\nu_{\ell_1}) \approx M_\ell^2/M(W_2)$$

$$M(\nu_{\ell_2}) \approx M(W_2)$$

and mixing angle $$\delta \sim M_\ell/M(W_2)$$

Here the small mass of the predominantly left-handed neutrino ν_1 is clearly related to the suppression of the right-handed currents through the asymmetric vacuum expectation values $\langle\Delta_L\rangle = 0$ and $\langle\Delta_R^0\rangle = v$.

2.4 The Low-Energy Hamiltonian

In the case of Dirac neutrinos $m(\nu_R) = m(\nu_L)$, which is known experimentally to be small. The effective low-energy Hamiltonian for charged current processes is then

$$H_{eff} = \frac{g^2}{2M^2(W_1)} \{J_L J_L^\dagger(\cos^2\zeta + \varepsilon\sin^2\zeta) - J_R J_R^\dagger(\sin^2\zeta + \varepsilon\cos^2\zeta) + (J_L J_L^\dagger + J_R J_L^\dagger)(1-\varepsilon)\sin\zeta\cos\zeta\} \tag{2.1}$$

where the mass-squared ratio $\varepsilon \equiv M^2(W_1)/M^2(W_2)$ and the left-right mixing angle ζ are small. Retaining only the leading order terms

$$H_{eff} = \frac{g^2}{2M^2(W_1)} \{J_L J_L^\dagger + \varepsilon J_R J_R^\dagger + \zeta(J_L J_R^\dagger + J_R J_L^\dagger)\}$$

In the Majorana case described in section (2.3) the predominantly right-handed ν_2 is too massive to be produced in low-energy processes. The effective Hamiltonian is now different for leptonic and semileptonic processes since right-handed currents are suppressed by a factor of $\sin\delta$ at the leptonic vertices:

Semileptonic:

$$H_{eff} = \frac{g^2}{2M^2(W_1)} \{J_L J_L^\dagger \cos\delta(\cos^2\zeta + \varepsilon\sin^2\zeta) - J_R J_R^\dagger \sin\delta(\sin^2\zeta + \varepsilon\cos^2\zeta) + (J_R J_L^\dagger \cos\delta - J_L J_R^\dagger \sin\delta)(1-\varepsilon)\sin\zeta\cos\zeta\}$$

Leptonic:

$$H_{eff} = \frac{g^2}{2M^2(W_1)} \{J_L J_L^\dagger \cos^2\delta(\cos^2\zeta + \varepsilon\sin^2\zeta) + J_R J_R^\dagger \sin^2\delta(\sin^2\zeta + \varepsilon\cos^2\zeta) - (J_R J_L^\dagger + J_L J_R^\dagger)(1-\varepsilon)\sin\delta\cos\delta\sin\zeta\cos\zeta\}$$

Then to leading order in ε and ζ, but neglecting terms in δ:

Semileptonic: $$H_{eff} = \frac{g^2}{2M^2(W_1)} \{J_L J_L^\dagger + \zeta J_R J_R^\dagger\}$$

where the right-handed current is purely hadronic.

Leptonic: $$H_{eff} = \frac{g^2}{2M^2(W_1)} J_L J_L^\dagger$$

Thus if the ν_2 are sufficiently massive, purely leptonic low-energy processes such as muon decay give no information on ε and ζ regardless of $M(W_2)$, while semileptonic processes still yield information on ζ. The non-leptonic low-energy Hamiltonian is unchanged from equation (2.1).

2.5 Limits on Right-Handed Currents

The already exisitng experimental 90% confidence limits on the mass-squared ratio ε and the mixing angle ζ are displayed in Figure (2.1). The allowed regions are those which include $\varepsilon=\zeta=0$, i.e. the (V-A) limit. Only the limits from the y distributions in νN and $\bar{\nu}N$ scattering (double lines, Ref. 16) are valid irrespective of the ν_R mass. The other limits assume massless or very light ν_R. Muon decay contours are derived from decay-rate measurements opposite the μ^+ spin direction at the spectrum endpoint (bold curve, spin-held data from the present experiment, Ref. 9); the product of the asymmetry parameter and the μ^+ polarization, ξP_μ (dotted curve, Ref. 17); and the Michel parameter ρ (solid curve, Ref. 18). Nuclear β decay contours are obtained from the Gamow-Teller β polarization (dot-dashed curves, Ref. 19); the comparison of Gamow-Teller and Fermi β polarizations (long-dashed curves, Ref. 20); and the ^{19}Ne asymmetry A(0) and ft ratio, with the assumption of conserved vector current (short-dashed curves, Refs. 21 and 22).

Additional model dependent limits, independent of the ν_R mass but assuming the same left- and right-handed quark mixing angles, are set by semileptonic decays[23] $[|\zeta|(1-\varepsilon)<0.005]$, current algebra analysis of non-leptonic $\Delta S=1$ weak decays[24] $[|\zeta|(1-\varepsilon)<0.004$, and $M(W_2)>300$ GeV if $\zeta=0]$, and the K_L-K_S mass difference[25,26] $[M(W_2)>1.6$ TeV$]$. Without the quark mixing angle assumption the K_L-K_S mass difference provides a general limit[27] $M(W_2)>300$ GeV.

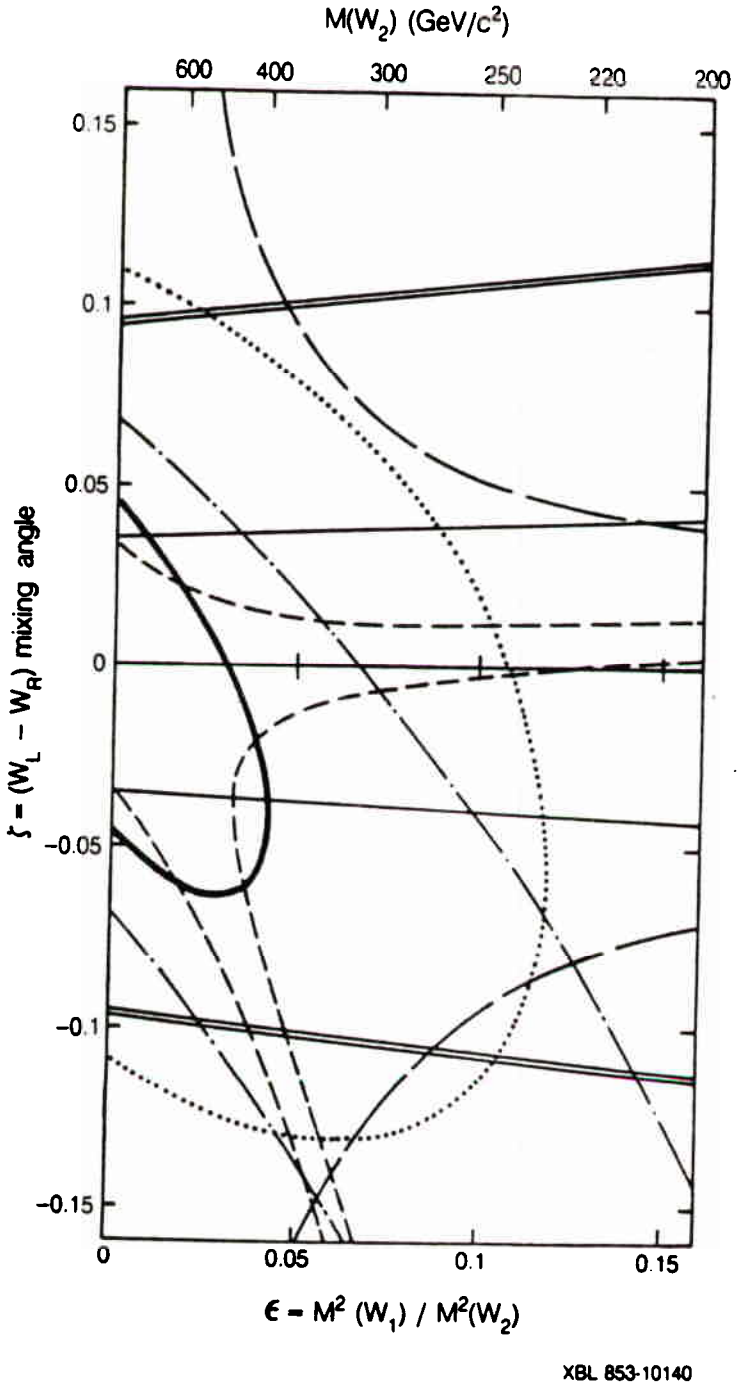

FIGURE (2.1). Experimental 90% confidence limits on the $W_{1,2}$ mass-squared ratio ϵ and the left-right mixing angle ζ. The allowed regions are those which include $\epsilon=\zeta=0$. The sources of the limits are described in the text.

Chapter 3

Muon Decay

3.1 Four-Fermion Contact Interaction

The muon differential decay rate for an interaction mediated by a heavy vector boson, W, differs from that for the corresponding four-fermion contact interaction by terms[28] of order $(m_\mu/M_W)^2$. These terms are $\sim 10^{-6}$ for $M_W \approx 80$ GeV/c^2 and are negligible at the present level of experimental precision. Consequently it is legitimate to treat muon decay as a contact interaction.

The μ^+ decay probability, integrated over e^+ spin directions, for the most general four-fermion contact interaction with massless neutrinos and in the absence of radiative corrections is[29,30]

$$\frac{d^2\Gamma}{dx\,d(\cos\theta)} \propto (x^2-x_0^2)^{1/2}\{9x(1-x) + 2\rho(4x^2-3x-x_0^2) + 9\eta x_0(1-x) + \xi\cos\theta(x^2-x_0^2)^{1/2}[3(1-x) + 2\delta(4x-3-m_e x_0/m_\mu)]\} \tag{3.1}$$

Here θ is the angle between the μ^+ spin direction and the e^+ momentum direction in the μ^+ rest frame, x is the standard reduced energy variable $x = E_e/E_e(\max)$ where $E_e(\max) = (m_\mu^2-m_e^2)/2m_\mu = 52.831$ MeV, and $x_0 = m_e/E_e(\max)$. The values of the muon decay parameters[29,30] ρ, η, ξ, and δ depend on the relative strengths of the scalar, pseudoscalar, vector, axial-vector and tensor interactions allowed by Lorentz invariance. Table (3.1) shows the (V-A) and (V+A) values of the decay parameters, together with their already existing experimental values[31]. The values assumed by the parameters for more general forms of the interaction are discussed in section (3.5).

Decay Parameter	(V-A) Value	(V+A) Value	Experimental Value
ρ	3/4	3/4	0.7517 ± 0.0026
η	0	0	0.06 ± 0.15
ξ	1	-1	ξP_μ: 0.972 ± 0.14 *
			$\xi P_\mu \delta/\rho$: >0.9959 (90% C.L.)
δ	3/4	3/4	0.7551 ± 0.0085

* P_μ is the muon longitudinal polarization from π^+ decay at rest.

Table (3.1)

3.2 Muon Decay Asymmetry

In this section the muon decay asymmetry for arbitrary values of the decay parameters is compared to the (V-A) prediction and is then related to the parameters ε and ζ which characterize the left-right symmetric model.

From here on the term involving η is assumed to be negligible. In addition to η being small experimentally [Table (3.1)], the term is suppressed by the factor $x_0 \approx 0.01$ and vanishes at the momentum spectrum endpoint. To simplify the discussion further the approximation $m_e = 0$ is made temporarily, yielding

$$\frac{d^2\Gamma}{dx\,d(\cos\theta)} \propto x^2\{9(1-x) + 2\rho(4x-3) + \xi\cos\theta[3(1-x) + 2\delta(4x-3)]\} \qquad (3.2)$$

If the μ^+ spin direction is precessed in a magnetic field the rate at which e^+ are emitted in a fixed direction becomes time-dependent through the time-dependence of $\cos\theta$. The instantaneous decay rate,

normalized to the time-averaged ($\cos\theta=0$) rate, is

$$R[x,\theta(t)] = 1 + \frac{3(1-x) + 2\delta(4x-3)}{9(1-x) + 2\rho(4x-3)}\,\xi\cos\theta(t)$$

The corresponding normalized rate for a purely (V-A) interaction ($\rho=\delta=3/4$, $\xi=1$) is

$$R[x,\theta(t)]_{(V-A)} = 1 + \frac{2x-1}{3-2x}\cos\theta(t)$$

The maximum time variation of the rate, and hence the greatest experimental sensitivity to the degree of parity violation, is attained at $x=1$ and for maximal variations of $\cos\theta(t)$. The spin-precessing magnetic field should therefore be perpendicular to the μ^+ spin direction. The decays of most interest are those in which the e^+ is emitted with x near 1 in a direction close to the μ^+ spin precession plane.

The amplitude of the resulting μSR signal, normalized to that expected for pure V-A muon decay, is

$$A(x) = \frac{R[x,\theta(t)] - 1}{R[x,\theta(t)]_{(V-A)} - 1}$$

and with the definitions $\tilde{x} = 1-x$, $\tilde{\delta} = 1-4\delta/3$ and $\tilde{\rho} = 1-4\rho/3$

$$A(\tilde{x}) = (\xi\delta/\rho)\{1 + 2\tilde{x}[\tilde{\delta}/(1-2\tilde{x}) - 3\tilde{\rho}/(1+2\tilde{x})]\} \qquad (3.3)$$

In the (V±A) limits $A(\tilde{x}) = \mp 1$. For small $\tilde{x}$ the (V-A) values of ρ and δ may be inserted into equation (3.2) provided ξ is then replaced by $A(\tilde{x})$.

An additional modification to equation (3.2) is required because the incoming μ^+ spin direction cannot be observed experimentally. However, in the (V-A) limit with massless neutrinos angular momentum

conservation requires the μ^+ from π^+ decay at rest to be emitted with their spin and momentum directions anti-parallel. Deviations from this limit can only reduce the longitudinal polarization P_μ. With θ redefined to be the angle between the observed μ^+ and e^+ momenta, equation (3.2) becomes

$$\frac{d^2\Gamma}{dx\,d(\cos\theta)} \propto x^2\{3-2x + P_\mu A(\tilde{x})\cos\theta(1-2x)\} \qquad (3.4)$$

The quantity $P_\mu A(\tilde{x})$ is the amplitude of the μSR signal normalized to that expected for (V-A) decay of μ^+ with $P_\mu=1$. In the context of left-right symmetric theories values of $P_\mu A(\tilde{x})<1$ imply the existence of right-handed currents or $m(\nu_\mu)>0$.

The remainder of this section is devoted to relating $P_\mu A(\tilde{x})$ to the mass-squared ratio $\varepsilon = M^2(W_1)/M^2(W_2)$ and mixing angle ζ of the left-right symmetric model. Following Beg et al.[32], the effective low-energy Lagrangian may be written as

$$L_{eff} = -(G/\sqrt{2})[V_\lambda{}^\dagger V^\lambda + \eta_{aa} A_\lambda{}^\dagger A^\lambda + \eta_{av}(V_\lambda{}^\dagger A^\lambda + A_\lambda{}^\dagger V^\lambda)]$$

where V and A are the vector and axial-vector parts of J_L and J_R. With $M_1 = M(W_1)$, and $M_2 = M(W_2)$:

$$G/\sqrt{2} = (g^2/8M_1^2)(\cos\zeta-\sin\zeta)^2 + (g^2/8M_2^2)(\cos\zeta+\sin\zeta)^2$$
$$\eta_{aa} = (\kappa^2 M_2^2 + M_1^2)/(\kappa^2 M_1^2 + M_2^2)$$
$$\eta_{av} = -\kappa(M_2^2 - M_1^2)/(\kappa^2 M_1^2 + M_2^2)$$
$$\kappa = (1+\tan\zeta)/(1-\tan\zeta)$$

The muon decay parameters are now:

$$\rho = (3/8)[(1+\eta_{aa})^2+4\eta_{av}^2]/[1+\eta_{aa}^2+2\eta_{av}^2]$$

$$\eta = 0$$

$$\xi = -2\eta_{av}(1+\eta_{aa})/[1+\eta_{aa}^2+2\eta_{av}^2]$$

$$\delta = 3/4.$$

and to leading order $\xi\delta/\rho = 1-2\varepsilon^2$

$$\tilde{\rho} = 2\zeta^2$$

The μ^+ from π^+ decay at rest have the polarization characteristic of Gamow-Teller β decay:

$$P_\mu = -2(\eta_{aa}/\eta_{av})/[1+(\eta_{aa}/\eta_{av})^2] = 1-2(\varepsilon+\zeta)^2$$

Equation (3.3) may now be rewritten in terms of ε and ζ:

$$P_\mu A(\tilde{x}) = 1 - 2\{2\varepsilon^2 + 2\varepsilon\zeta + \zeta^2[1 + 6\tilde{x}/(1+2\tilde{x})]\} \qquad (3.5)$$

Each value of $P_\mu A(\tilde{x})<1$ is associated with an elliptical contour in the real ε-ζ plane. Thus measurement of $P_\mu A(\tilde{x})$ constrains both ε and ζ.

3.3 Radiative Corrections

Radiative corrections to muon decay have been evaluated in detail only to order α. The first-order corrections are given by the virtual photon diagrams in Figure (3.1)(a)-(c) and the inner bremsstrahlung diagrams (d) and (e) corresponding to the radiative decay $\mu \to e\nu\bar{\nu}\gamma$. Fischer and Scheck[33] have calculated the radiative corrections for (V-A) decay in the case where the electron polarization is not summed over. The corrections independent of electron spin direction are unchanged if the (V-A) interaction is replaced by a more general vector and axial-vector interaction in charge retention form. Florescu and

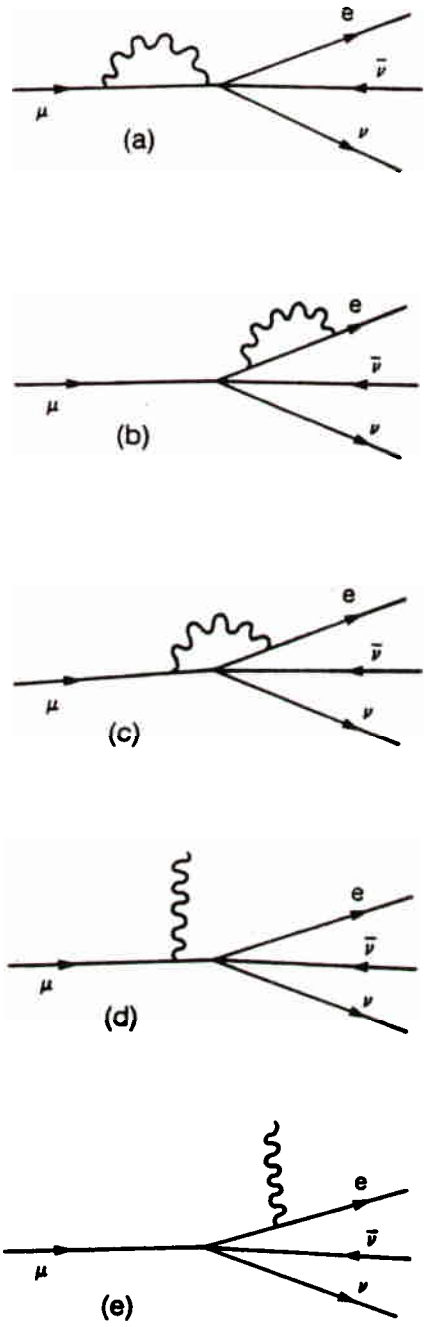

FIGURE (3.1). First-order radiative corrections to muon decay from virtual photon diagrams (a)-(c), and internal bremsstrahlung diagrams (d) and (e).

Kamei[34] have calculated radiative corrections for a general Fermi interaction. Including order α radiative corrections for (V-A) decay and finite electron mass equation (3.4) becomes[29,30]

$$\frac{d^2\Gamma}{dx\,d(\cos\theta)} \propto (1-x_0^2/x^2)^{1/2}\{[x^2(3-2x-x_0^2/x) + f_C(x)] + P_\mu A(\tilde{x})(1-x_0^2/x^2)^{1/2}[x^2(1-2x+m_e x_0/m_\mu) + f_\theta(x)]\cos\theta\} \tag{3.6}$$

where

$$f_C(x) = (\alpha/2\pi)x^2\{2(3-2x-x_0^2/x)R(x) - 3\ell nx + [(1-x)/3x^2][(5+17x-34x^2)\ell n(m_\mu x/m_e) + 2x(17x-11)]\} \tag{3.7}$$

$$f_\theta(x) = (\alpha/2\pi)x^2\{2(1-2x+m_e x_0/m_\mu)R(x) - \ell nx - [(1-x)/3x^2][(1+x+34x^2)\ell n(m_\mu x/m_e)+3-7x-32x^2+4(1-x)^2\ell n(1-x)/x]\} \tag{3.8}$$

$$R(x) = [\ell n(m_\mu x/m_e)-1][2\ell n(x^{-1}-1)+3/2] + \ell n(1-x)[\ell nx+1-x^{-1}] - \ell nx + 2L_2(x) - \pi^2/3 - 1/2 \tag{3.9}$$

and the Spence function $L_2(x) = -\int_0^x t^{-1}\ell n(1-t)dt$.

It should be noted that R(x), and hence $f_C(x)$ and $f_\theta(x)$, diverge logarithmically as $x\to1$. Qualitatively, the infrared divergences in the virtual photon diagrams are no longer compensated by those of the inner bremsstrahlung diagrams since the phase space for radiative decay vanishes as $x\to1$. These divergences may be eliminated by including multiple soft-photon emission. The main effect near x=1 is to replace $1+(2\alpha/\pi)[\ell n(m_\mu/m_e)-1]\ell n(1-x)$ in R(x) [equation (3.9)] by[30]

$$\exp[(2\alpha/\pi)[\ell n(m_\mu/m_e)-1]\ell n(1-x) = (1-x)^{(2\alpha/\pi)[\ell n(m_\mu/m_e)-1]}$$

which vanishes as $x\to1$ instead of diverging. It follows that an approximate correction of order α^2 may be made near x=1 by replacing

R(x) with

$$R_2(x) = R(x) + (2\alpha/\pi)\{\ln(1-x)[\ln(m_\mu/m_e)-1]\}^2 \qquad (3.10)$$

although, of course, $R_2(x)$ still diverges as $x \to 1$.

The data analysis uses equation (3.6) together with the radiative corrections of equations (3.7) through (3.10) to represent the μ^+ differential decay rate. Figure (3.2) shows the resulting e^+ momentum spectra parallel and anti-parallel to the μ^+ spin. The radiative corrections are clearly not negligible.

3.4 Effects of Intermediate Vector Bosons

As noted in section (3.1) the μ^+ differential decay rates for the (V-A) contact interaction and the W_L-mediated interaction differ by terms of order $(m_\mu/M_W)^2$. The effect may be approximated by modifying the decay parameters as[28]

$$\xi_W = 1 + 3m_\mu^2/5M_W^2$$

$$\rho_W = 3/4 + m_\mu^2/3M_W^2$$

and the decay rate as $\tau_W^{-1} = \tau^{-1}(1 + 3m_\mu^2/5M_W^2)$

In addition the order α radiative corrections contain extra terms[35] of order $\alpha(m_\mu/M_W)^2$. These effects are all negligible in the present experiment.

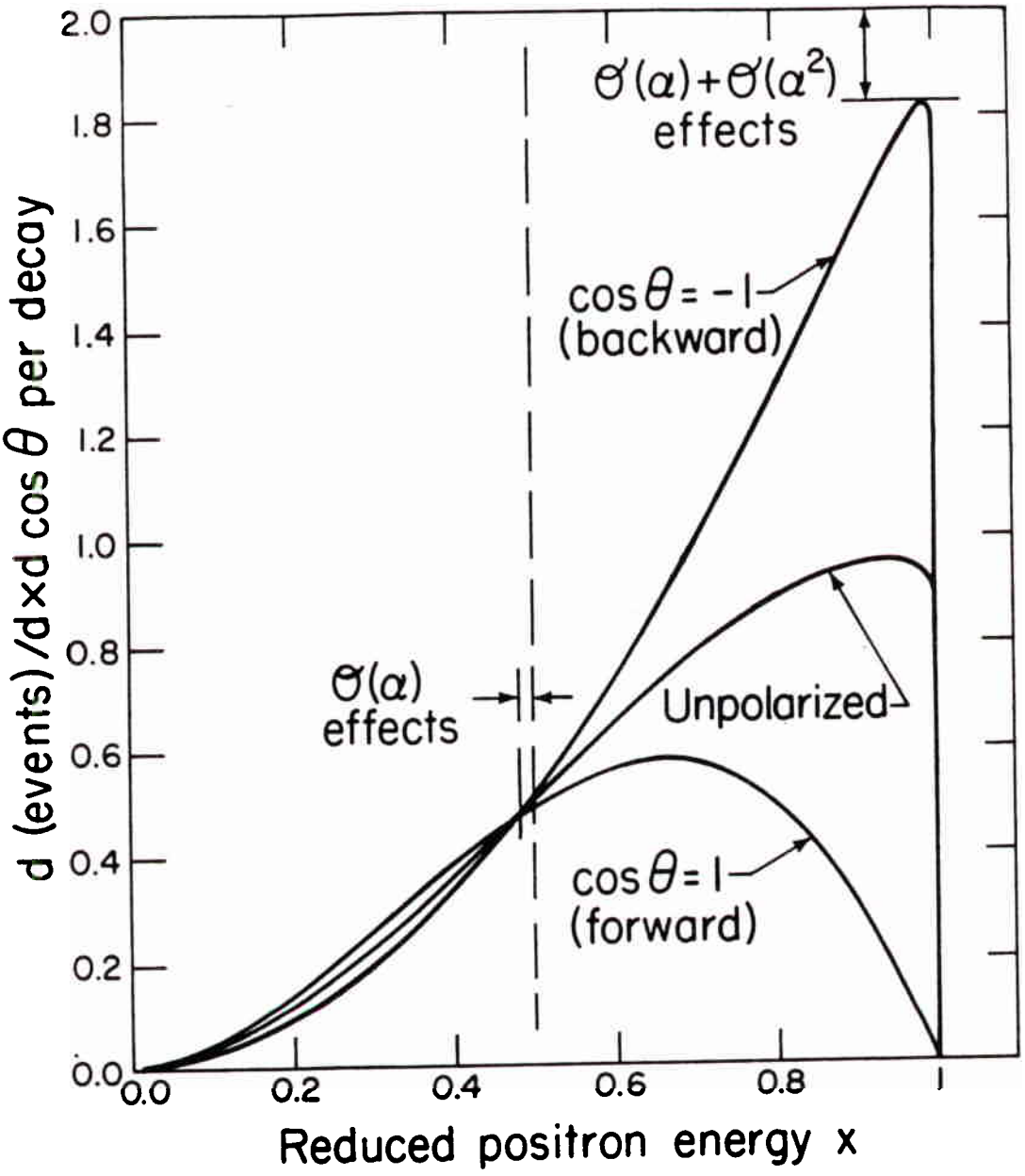

FIGURE (3.2). The (V-A) μ^+ differential decay rate parallel (backward) and anti-parallel (forward) to the μ^+ spin direction, and for unpolarized μ^+. The effects of radiative corrections are also indicated.

3.5 Lorentz Structure

Mursula and Scheck[36] have recently obtained limits on non-(V-A) couplings using a helicity projection form of the muon decay flavor retention contact interaction:

$$\begin{aligned} H = (G_0/\sqrt{2})\{&h_{11}(s+p)_{e\nu_e}(s+p)_{\nu_\mu\mu} + h_{12}(s+p)(s-p) + h_{21}(s-p)(s+p) \\ &+ h_{22}(s-p)(s-p) + g_{11}(v^\alpha+a^\alpha)(v_\alpha+a_\alpha) + g_{12}(v^\alpha+a^\alpha)(v_\alpha-a_\alpha) \\ &+ g_{21}(v^\alpha-a^\alpha)(v_\alpha+a_\alpha) + g_{22}(v^\alpha-a^\alpha)(v_\alpha-a_\alpha) \\ &+ f_{11}(t^{\alpha\beta}+t'^{\alpha\beta})(t_{\alpha\beta}+t'_{\alpha\beta}) + f_{22}(t^{\alpha\beta}-t'^{\alpha\beta})(t_{\alpha\beta}-t'_{\alpha\beta}) + \text{h.c.}\} \end{aligned} \tag{3.11}$$

where $s_{ik} = \bar{\psi}_i 1 \psi_k$, $p_{ik} = \bar{\psi}_i \gamma_5 \psi_k$, $v^\alpha_{ik} = \bar{\psi}_i \gamma^\alpha \psi_k$, $a^\alpha_{ik} = \bar{\psi}_i \gamma^\alpha \gamma_5 \psi_k$, $t^{\alpha\beta}_{ik} = \bar{\psi}_i (\sigma^{\alpha\beta}/\sqrt{2}) \psi_k$, $t'^{\alpha\beta}_{ik} = \bar{\psi}_i (\sigma^{\alpha\beta}\gamma_5/\sqrt{2}) \psi_k$ and the particle indices are as indicated in the h_{11} term.

The pure (V-A) interaction is very simple in this form: only $g_{22}\neq 0$. The combinations of covariants in each term project onto states of definite helicity in the limit of massless particles, and eliminate interference terms except between (scalar ± pseudoscalar) and tensor interactions.

The deviations of the muon decay parameters from their (V-A) values are

$$\rho - 3/4 = -(12/A)\{|g_{12}|^2+|g_{21}|^2+2|f_{11}|^2+2|f_{22}|^2+\text{Re}(h_{11}f_{11}^*+h_{22}f_{22}^*)\}$$

$$\delta - 3/4 = (36/A\xi)\{|g_{12}|^2-|g_{21}|^2-2|f_{11}|^2+2|f_{22}|^2-\text{Re}(h_{11}f_{11}^*-h_{22}f_{22}^*)\}$$

$$\xi - 1 = -(8/A)\{4(|g_{11}|^2+2|g_{12}|^2-|g_{21}|^2)+|h_{11}|^2+|h_{21}|^2-4|f_{11}|^2+16|f_{22}|^2 - 8\text{Re}(h_{11}f_{11}^*-h_{22}f_{22}^*)\}$$

$$\eta = (8/A)\text{Re}[g_{21}(h_{22}^*+6f_{22}^*)+g_{12}(h_{11}^*+6f_{11}^*)+g_{22}h_{21}^*+g_{11}h_{12}^*]$$

where $$A = 4\{4(|g_{22}|^2+|g_{11}|^2+|g_{12}|^2+|g_{21}|^2)+|h_{11}|^2+|h_{12}|^2+|h_{21}|^2+|h_{22}|^2 + 12(|f_{11}|^2+|f_{22}|^2)\}$$

The couplings are related to equation (3.3) by equation (3.12):

$$A(0) = \xi\delta/\rho = 1 - \frac{8|g_{11}|^2+2|h_{21}|^2+2|h_{11}-2f_{11}|^2}{4(|g_{11}|^2+|g_{22}|^2)+|h_{12}|^2+|h_{21}|^2+|h_{11}-2f_{11}|^2+|h_{22}-2f_{22}|^2}$$

Measurement of $P_\mu A(0) \leq A(0)$ therefore allows limits to be set on the couplings g_{11}, h_{11}, h_{21}, and f_{11}. Limits from the present experiment are presented in section (9.6).

Several constraints are imposed on the couplings if it is assumed that (i) the charged weak interactions are mediated by heavy bosons with spin 0, 1, or 2, (ii) the vector and tensor boson couplings are e-μ universal, and (iii) the scalar boson coupling may instead be proportional to the lepton mass (weak universality):

h_{12}, h_{21} real, positive semi-definite

$h_{22}=h_{11}^*$ with $|h_{11}|^2=h_{12}h_{21}$

g_{11}, g_{22} real, positive semi-definite

$g_{21}=g_{12}^*$ with $|g_{12}|^2=g_{11}g_{22}$

$f_{22}=f_{11}^*$

Limits on g_{11}, h_{11}, h_{21}, and f_{11} therefore constrain other couplings. It should also be noted that any deviation of δ from 3/4 would indicate a violation of e-μ universality.

Two special cases are of interest:

1) In the standard electroweak model where the charged weak interaction is mediated by a single heavy vector boson $W^\pm$ which couples universally

$$A(0) = 1 - 2|g_{11}|^2/(|g_{11}|^2+|g_{22}|^2)$$

and more significantly $\quad P_\mu = (g_{22}-g_{11})/(g_{22}+g_{11})$

so that $$P_\mu A(0) = 1 - 2g_{11}/g_{22}$$

2) In the context of the left-right symmetric model g_{11} and g_{12} provide measures of ϵ and ζ.

Chapter 4

Muons in Matter

4.1 Muon Deceleration and Thermalization

The deceleration and thermalization of μ^+ in matter has been reviewed by Brewer et al.[37] The main energy-loss processes depend on the μ^+ energy. For kinetic energies E>2-3 keV the energy loss is by scattering with electrons. The μ^+ beam is partially depolarized through spin exchange with the unpolarized electrons of the medium[38]. The calculation in section (4.2) shows the depolarization to be 7×10^{-4} for surface muons. In addition, multiple Coulomb scattering from nuclei, which is non-relativistically spin conserving, misaligns the μ^+ spin and momentum directions. At E≈2-3 keV the μ^+ velocity is comparable to that of the valence electrons of the medium. The μ^+ then begin to capture and lose electrons rapidly, forming a succession of short-lived muonium (μ^+e^-) states. Again energy is lost in collisions with electrons. Below E≈200 eV stable muonium is formed, and the energy loss is due to collisions of muonium with atoms and molecules. The time spent by the decelerating μ^+ in muonium states is too short for the hyperfine transitions to cause any appreciable depolarization.

In many non-metals the μ^+ are thermalized as muonium. In others, muonium with E≈1-20 eV participates in 'hot atom' reactions where the μ^+ become incorporated into molecules. The stopping targets in the present work were either metals or liquid helium. The μ^+ are thermalized in metals in a quasi-free state because the high conduction electron concentration effectively screens the μ^+ from interactions with individual electrons. In liquid He the energetically favored final

Subject: Re: thesis
Date: Fri, 06 Aug 1999 11:33:12 -0700 (PDT)
From: David Stoker <stoker@SLAC.Stanford.EDU>
To: David Gill <drgill@triumf.ca>

Hi Dave,
Section 4.2 of my thesis is incorrect due to a mis-interpretation of the paper by Ford and Mullin. There is an erratum (Phys. Rev D37, 237, (1988)) to our paper by Jodidio et al. (Phys. Rev. D34, 1967 (1986)). You may also find a typo E**2 = p**2 - m**2 somewhere!

Dave

state is the molecular ion $He\mu^+$ with binding energies[39] of 1.9 eV for the ground state and 1.2 eV for the first vibrational state. Muonium is strongly disfavored in the final state due to the large difference between the ionization potentials of helium (24.6 eV) and muonium (13.5 eV). However, if any muons are thermalized as muonium they may survive in this form for a considerable time because of the improbability of encountering a He^+ ion with which to recombine as $He^+ + \mu^+e^- \rightarrow He\mu^+$.

4.2 Muon Depolarization in Scattering from Unpolarized Electrons

Ford and Mullin[38] have shown that when non-relativistic μ^+, with velocity β in the laboratory frame, scatter with unpolarized e^- through a center of mass angle θ the probability that the final μ^+ spin direction is parallel ($\varepsilon=1$) or anti-parallel ($\varepsilon=-1$) to the initial spin direction is:

$$Q(\varepsilon,\theta) = \frac{1+\varepsilon}{2} - \varepsilon \frac{m^2}{\mu^2} \beta^4[\sin^2(\theta/2) - \sin^4(\theta/2) + \sin^6(\theta/2)]$$

where $m=m_e$ and $\mu=m_\mu$.

If the muons are initially fully polarized the final polarization after one scatter through θ is

$$P_\mu = 1 - 2 \frac{m^2}{\mu^2} \beta^4[\sin^2(\theta/2) - \sin^4(\theta/2) + \sin^6(\theta/2)]$$

The corresponding fractional energy loss is

$$w = \frac{m}{\mu} \beta^2 \sin^2(\theta/2).$$

With $\Delta P_\mu = 1-P_\mu$ the 'depolarizing power' of a given fractional energy loss is

$$\frac{\Delta P_\mu}{w} = 2\frac{m}{\mu}\beta^2[1 - \sin^2(\theta/2) + \sin^4(\theta/2)]$$

and

$$\frac{d}{d[\sin^2(\theta/2)]}\frac{\Delta P_\mu}{w} = 2\frac{m}{\mu}\beta^2[-1 + 2\sin^2(\theta/2)]$$

The depolarization per unit energy loss is maximized for $\theta\to 0$ and π, and is reduced by 25% at the $\theta=\pi/2$ minimum. In the non-relativistic limit the scattering cross section $\sigma \sim \mathrm{cosec}^4(\theta/2)$. Then considering only small angle scattering the polarization after one scatter is

$$P_\mu = 1 - 2\frac{m^2}{\mu^2}\beta^4\sin^2(\theta/2)$$

with corresponding energy-loss

$$dE = -Ew = -\mu(\gamma-1)w = -m(\gamma-1)\beta^2\sin^2(\theta/2)$$

The number of such scatters resulting in an energy loss δE such that $dE \ll \delta E \ll E$ is

$$N = \frac{\delta E}{dE} = \frac{\delta E}{m(\gamma-1)\beta^2\sin^2(\theta/2)}$$

and the polarization is then

$$P_\mu(\delta E) = [1 - 2\frac{m^2}{\mu^2}\beta^4\sin^2(\theta/2)]^N$$

$$= 1 - 2\frac{m^2}{\mu^2}\frac{\beta^2}{\gamma-1}\delta E$$

$$= 1 - 2\frac{m}{\mu^2}\frac{\gamma+1}{\gamma^2}\delta E$$

The depolarization of non-relativistic (γ=1) muons is therefore almost independent of their energy and proportional to their energy loss. Surface muons initially have E=4.1 MeV and γ=1.04. Using ΔE=4.1Mev and γ=1.02 the depolarization when the μ^+ are (almost) brought to rest is

$$1 - P_\mu = 2 \frac{m}{\mu^2} \frac{\gamma+1}{\gamma^2} \Delta E = 7.3 \times 10^{-4}$$

4.3 Spin-Lattice Relaxation

In order to obtain the most precise value of the measured muon mean-life τ_μ to use in fitting the μSR data one would like to include information from the spin-held mode of the experiment. However, muon spin-lattice relaxation in the spin-held mode conspires with parity violation to change the measured τ_μ from its true value.

It should first be pointed out that while the 1.1-T spin-holding field is sufficient to quench μ^+ depolarization in muonium, it cannot 'hold' the spins of quasi-free muons in the metal targets. The energy difference between states where the muon spin is parallel and anti-parallel to the 1.1-T field is only $\Delta E = 6.2 \times 10^{-7}$ eV, whereas the room temperature thermal energy is $kT = 2.6 \times 10^{-2}$ eV. Relaxation of the muon spins toward the equilibrium situation, where the numbers of spins anti-parallel and parallel to the applied field are almost equal, requires the presence of oscillating magnetic fields with frequency $\omega = 9 \times 10^8$ s^{-1}. Such fields are provided by the nuclear magnetic dipole moments and the lattice vibrations associated with low frequency acoustic phonons. The stopped muon polarization decays exponentially toward thermal equilibrium with the characteristic spin-lattice

relaxation time constant T_1.

Now consider a μ^+ with its spin anti-parallel to the beam direction. According to (V-A) theory the probabilty that the decay e^+ is emitted along the beam direction is enhanced by a factor of

$$E(x) = 1/2(1-x)$$

if the muon spin direction is reversed. The decay time spectrum becomes

$$N(x,t) = N_0 \exp(-t/\tau_\mu)\{\exp(-t/T_1) + E(x)[1-\exp(-t/T_1)]\}$$

If T_1 is much longer than the observation time the decay spectrum appears almost exponential with an effective measured muon mean-life τ_μ' given by:

$$\tau_\mu' = \frac{\tau_\mu T_1}{T_1 - [E(x)-1]\tau_\mu} \qquad (4.1)$$

Thus $\tau_\mu' > \tau_\mu$ for $x > 1/2$, and the effect increases rapidly as $x \to 1$.

The spin-held data from the second running period ('Run 2') with $x > 0.88$ is shown in Figure (4.1). The fitted muon mean-life is $\tau_\mu' = 2.214 \pm 0.004(\text{stat})$ μs and the fitted background of 1.2 ± 9.8 per time bin is consistent with zero.

Figure (4.2) shows the τ_μ' of the spin-held data fitted as a function of the decay e^+ momentum. The background, which was found to be consistent with zero throughout the x range, was fixed to zero. The Run 2 and Run 3 aluminum target data has been combined. Different μ^+ lifetime clocks were used in each of the three running periods, and the lower statistics Run 1 data has been omitted since it covered a shorter x range than the Run 2 and Run 3 data. The curves are fits to equation (4.1) with finite angular acceptance effects included in E(x) and

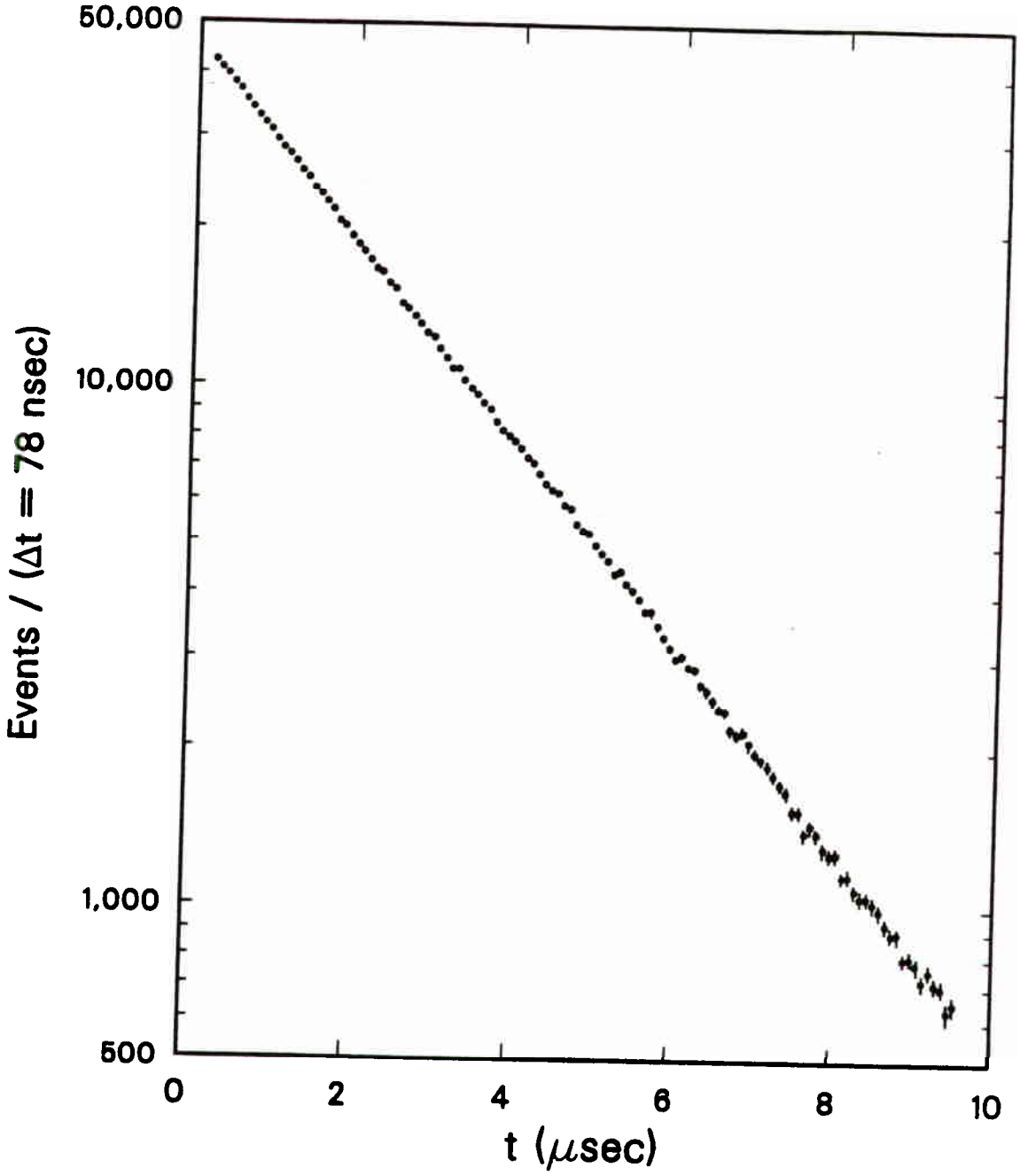

FIGURE (4.1). Time spectrum of the spin-held data from Run 2. The fitted muon mean-life is τ_μ=2.214±0.004(stat.) μs with a fitted background of 1.2±9.8 per time bin.

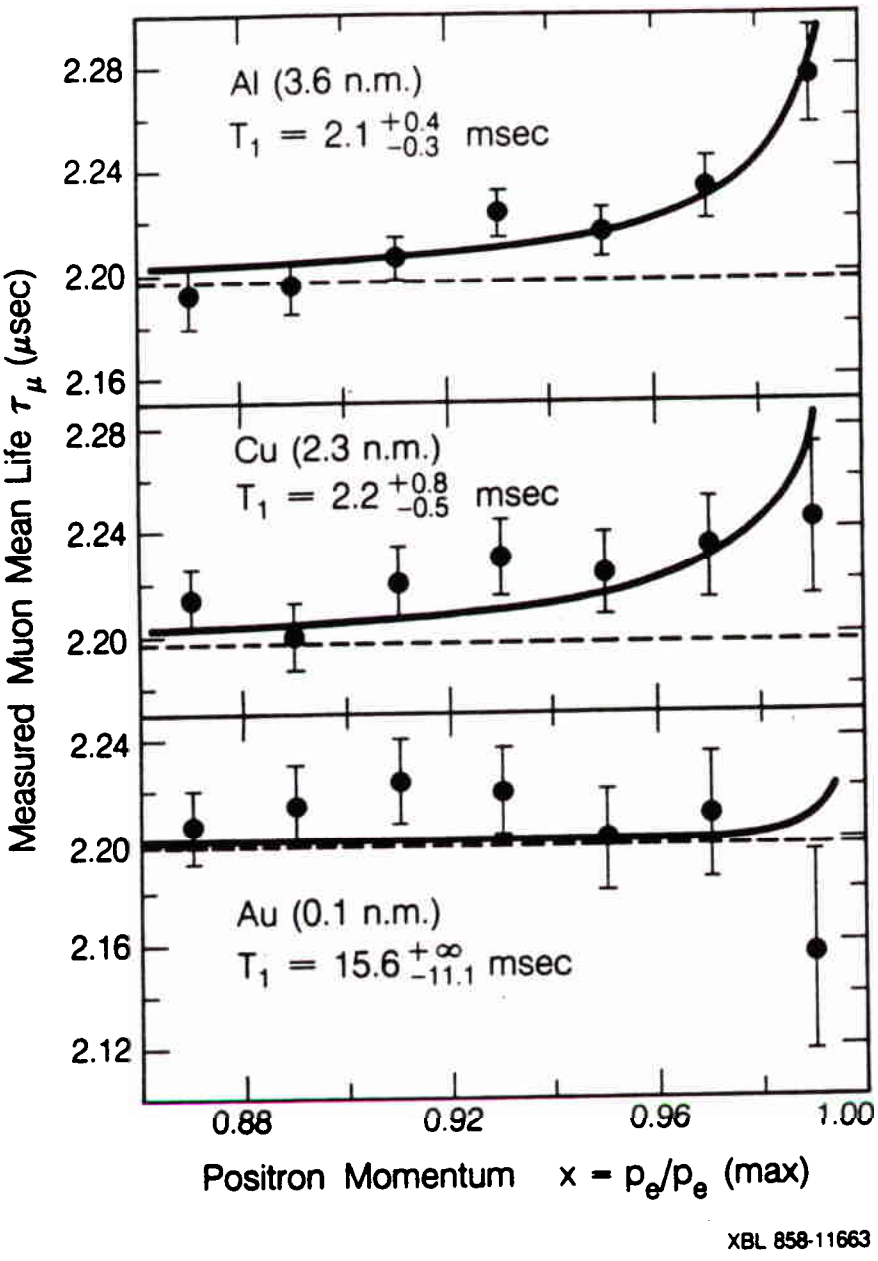

FIGURE (4.2). Fitted muon mean-life τ_μ' versus decay positron momentum for spin-held data from aluminum, copper, and gold targets. The target material nuclear magnetic moment in units of nuclear magnetons (n.m.) is indicated. The correlation between the putative spin-lattice relaxation times T_1 and the nuclear magnetic moments suggests a real spin-lattice relaxation effect.

assuming the true muon mean-life τ_μ=2.197 μs. The best fit spin-lattice relaxation time constants of $T_1=2.1^{+0.4}_{-0.3}$ ms for Al, $T_1=2.2^{+0.8}_{-0.5}$ ms for Cu, and $T_1=15.6^{+\infty}_{-11.1}$ ms for Au correlate with their respective nuclear dipole moments of 3.6, 2.3, and 0.1 nuclear magnetons. This correlation suggests the effect is due to spin-lattice relaxation rather than some residual background problem. In principle the foregoing method provides a means of measuring μ^+ spin-lattice relaxation time constants $T_1 \sim 10^3 \tau_\mu$.

In conclusion no spin-held data muon lifetime information is used in fitting the μSR data, which is time-average unpolarized, since the two data sets do not necessarily have the same apparent τ_μ.

4.4 Spin-Spin Relaxation: μSR Signal Damping

The spins of muons stopped in the target material precess under the combined influence of the external transverse magnetic field and the randomly oriented internal local fields produced mainly by the nuclear magnetic dipole moments. The muon spins therefore precess with slightly different Larmor frequencies resulting in a loss of phase coherence.

The decay of the spin phase coherence is observed experimentally as a damping, G(t), of the μSR signal amplitude. This is seen in Figure (4.3) which displays data from the second run period. Although the μSR signal damping can yield much information about the environment in which the μ^+ are brought to rest, it is clearly an unwelcome nuisance in an experiment where one would like to measure a μSR signal amplitude determined solely by the weak interaction. If the exact form of G(t) were known the desired amplitude would, in principle, be simply the time t=0 amplitude obtained from a fit to the μSR data. Unfortunately,

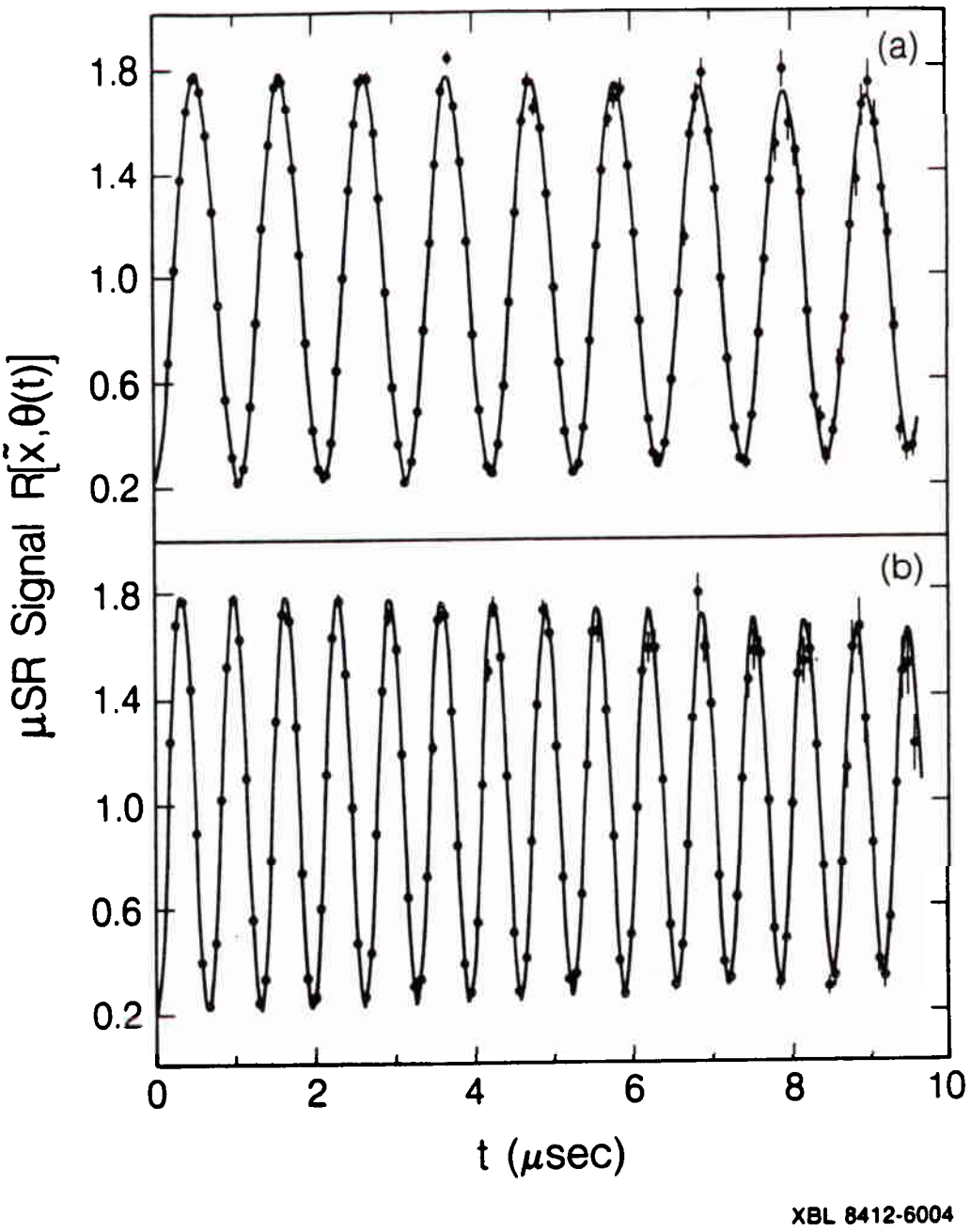

FIGURE (4.3). The μSR data from Run 2, contributing 73% of the total data base for the final results, with spin-precessing fields (a) B_T=70-G, and (b) B_T=110-G. The exponential decay with muon lifetime has been factored out. Spin-spin relaxation causes a damping of the μSR signal amplitude.

there is no 'magic formula' for G(t) which describes exactly the signal damping observed in real, i.e. imperfect, materials such as metals which contain, to some degree, impurities and lattice defects. However, it will be seen in the following discussion that approximate expressions for G(t) can be obtained if certain simplifying assumptions are made.

A wealth of general information about spin depolarization in μSR experiments can be found in the proceedings of recent topical conferences[40]. The recent review of transport mechanisms of light interstitials in metals by Richter[41] summarizes much useful information.

In metals with large nuclear dipole moments such as copper and aluminum the local dipole fields are a few Gauss at the interstitial lattice sites occupied by the muons. The μ^+ spin phase coherence decays according to the ensemble average

$$G(t)\exp(i\omega_0 t) = \langle \exp[i\int_0^t \omega(t')dt'] \rangle$$

where $\omega(t) = \omega_0 + \omega'(t)$ with ω_0 the Larmor frequency in the external field alone and $\omega'(t)$ the frequency shift due to dipolar interactions. An approximate analytic expression for G(t) can be obtained by assuming (i) that the frequency modulation $\omega'(t)$ is random, (ii) that it is a Gaussian random process so that only the second-order cumulant, or correlation function of $\omega'(t)$ with $\omega'(0)$, need be considered and (iii) that the correlation function decays exponentially with a correlation time τ_c characteristic of the time a μ^+ resides at a lattice site before diffusing to another. The correlation function becomes

$$\langle\omega'(t)\omega(0)\rangle = \langle\omega'(0)^2\rangle\exp(-t/\tau_c) = 2\sigma^2\exp(-t/\tau_c)$$

and then $$G(t) = \exp\{-2\sigma^2\tau_c^2[\exp(-t/\tau_c)-1+t/\tau_c]\} \qquad (4.2)$$

Equation (4.2) is the Kubo-Tomita[4,2] or motional-narrowing form of the spin relaxation function.

In the limiting case of immobile μ^+ $G(t,\tau_c\to\infty) = \exp(-\sigma^2t^2)$, while for extremely mobile μ^+ the local field fluctuations are averaged and motional-narrowing occurs: $G(t,\tau_c\to0) = \exp(-2\sigma^2\tau_c t)$. For intermediate values of τ_c equation (4.2) provides a useful interpolation between the Gaussian and exponential limits.

The static linewidth σ^2 is related to the random local dipole fields ΔB by

$$\sigma^2 = \gamma_\mu^2\langle\Delta B^2\rangle/2 \qquad (4.3)$$

where $\gamma_\mu = 8.5\times10^4$ radians/sec-G, and is given by the van Vleck formula[4,3]

$$\sigma^2 = (\hbar^2/6)\gamma_\mu^2\gamma_I^2 I(I+1)\sum_j(1-3\cos^2\theta_j)^2/r_j^6 \qquad (4.4)$$

where r_j is the distance of the μ^+ from the nuclear spin I_j, θ_j is the angle between $\hat{r}_j$ and the external field direction, and γ_μ and γ_I are the gyromagnetic ratios for the μ^+ and nuclei, respectively. Acccording to equation (4.4) σ^2 depends markedly on the crystal lattice orientation relative to the external field. However, for the small external fields used in the present experiment (≈100 G) the orientation dependence is reduced strongly by additional interactions between the nuclear quadrupole moments and the electric field gradient produced by

the muon.

The main shortcomings in the assumptions used to obtain G(t) in equation (4.2) are now considered. Kehr et al.[44] have shown that inclusion of only the second-order cumulant leads to a more rapid damping than that exhibited by their more general Markovian-random walk formulation. Although the precession frequency shifts ω' are different at each interstitial site there are correlations between the ω' at neighboring sites because the μ^+ is subject to some of the same nuclear spins. This effect can be treated approximately by using a correlation time τ_c longer than the mean μ^+ residence time at each site. In addition, since the μ^+ has been regarded as a classical particle localized at specific sites, possible delocalization effects have been neglected.

The preceding discussion has also ignored the possibility that μ^+ become trapped at lattice defects. The defects may be impurities such as oxygen or nitrogen atoms which trap μ^+ below about 80 K, lattice vacancies or dislocations which trap μ^+ up to about room temperature, or larger voids in which the surface electric dipole layer and image force can produce a deep trapping well[45]. Kehr et al.[44] have also constructed a Markovian-random walk theory of spin depolarization for diffusion in the presence of traps. They consider a two state model in which the μ^+ is either trapped for an average time τ_0 during which $G(t)=\exp(-\sigma^2t^2)$, which is the simplest approximation corresponding to muons at fixed sites in the traps, or is untrapped for an average time τ_1 during which G(t) is taken to be their result in the absence of traps. The contributing random walk processes are summed in integral equations which are solved by Laplace transform and inverted

numerically to yield G(t). It should be noted that the initial conditions are not equilibrium conditions since the μ^+ are stopped at random sites. If the concentration of traps is c then at time t=0 the fraction of μ^+ in traps is c, while under equilibrium conditions the fraction is $\tau_0/(\tau_0+\tau_1)$. At room temperature equilibrium should be established in times short compared to the mean μ^+ lifetime.

The observed μSR signal damping, in principle, has a small spin-lattice relaxation component. Any non-uniformities in the applied spin-precessing field B_T also contribute.

It should now be clear that the G(t) of equation (4.2) can provide only an approximation to the true form of the μSR signal damping. Therefore fitting the μSR data assuming equation (4.2) to be valid may lead to a fitted time t=0 amplitude either smaller or larger than the true amplitude. The approach taken in the data analysis discussed in Chapter 7 is to use the Gaussian limit of equation (4.2) and then try to show that this underestimates the true time t=0 amplitude. This procedure yields more conservative limits on right-handed currents.

Chapter 5

The Beamline and Apparatus

5.1 The Beamline

The TRIUMF M13 beamline[4,6] shown in Figure (5.1) is a low momentum (20-130 MeV/c) pion and muon channel viewing the 1AT1 production target at 135° with respect to the primary proton beam. The secondary beam is transported through two 60° bends, the first right and the second left, to a final focus (F3) nominally 9.4 m downstream of the production target. The symmetric quadrupole triplet (Q3-Q5) produces a relative inversion of the images at the intermediate foci F1 and F2, thereby yielding an achromatic focus at F3. The symmetric configuration of the beamline elements also suppresses second order effects and produces a magnification of unity at F3. The beam phase space is governed by the setting of the horizontal and vertical jaws (J) upstream of the first dipole (B1). The momentum bite is restricted by the horizontal components of slits SL1 and SL2 at the intermediate foci F1 and F2. With the exception of B1 in Run 1, the dipoles were NMR-monitored.

Figure (5.2) shows the positive particle fluxes obtained in the beam tuning studies of ref. (46). For data collection in the present experiment the beamline was tuned to 29.5 MeV/c, i.e. 1% below the 29.8 MeV/c surface muon edge. This allowed a 2% $\Delta p/p$ momentum bite during occasional periods of low primary proton flux, although a 1% $\Delta p/p$ was normally used. Under normal running conditions 100 μA of 500 MeV protons incident on a 2 mm thick carbon production target yielded 1.8×10^4 μ^+/sec at the stopping target. The μ^+ beam spot rms spatial and angular dimensions were typically 6 mm and 35 mrad

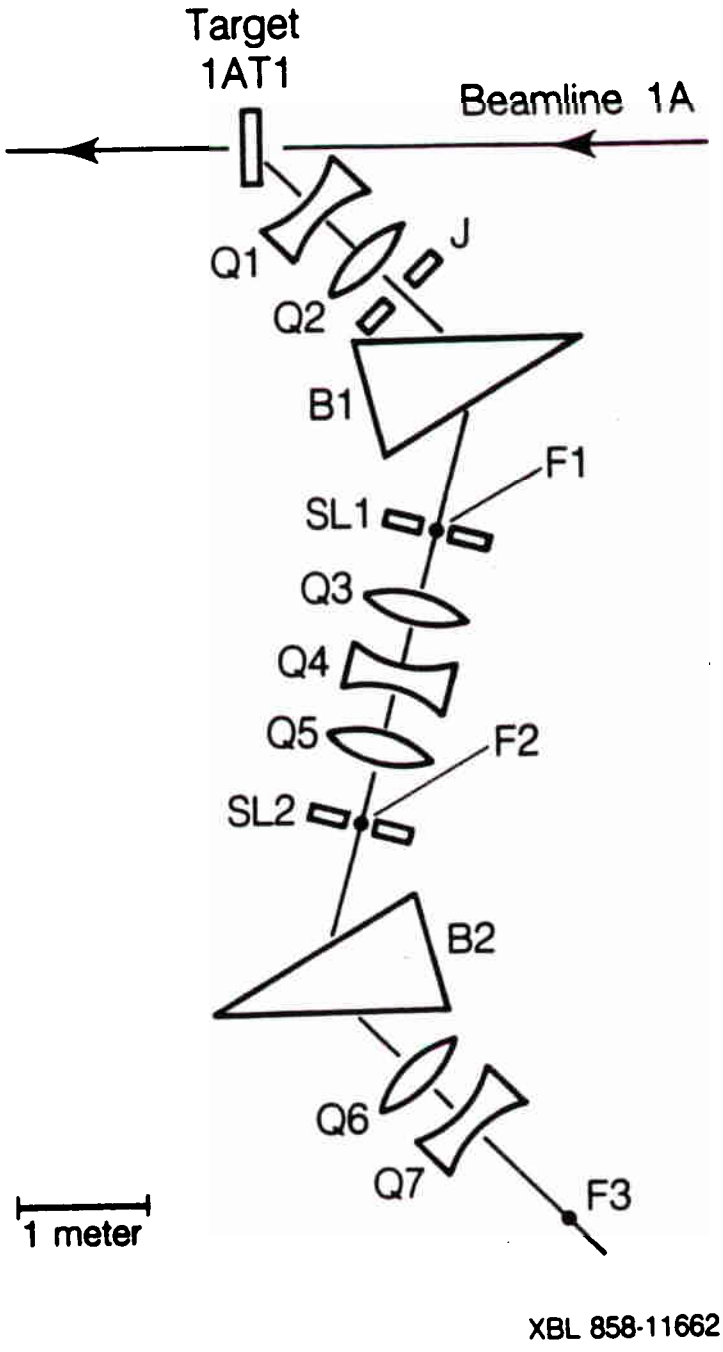

FIGURE (5.1). The TRIUMF M13 beamline. B1 and B2 are dipoles; Q1-Q7 are quadrupoles; F1-F3 are foci; the slits SL1 and SL2, and the jaws J have both horizontal and vertical components.

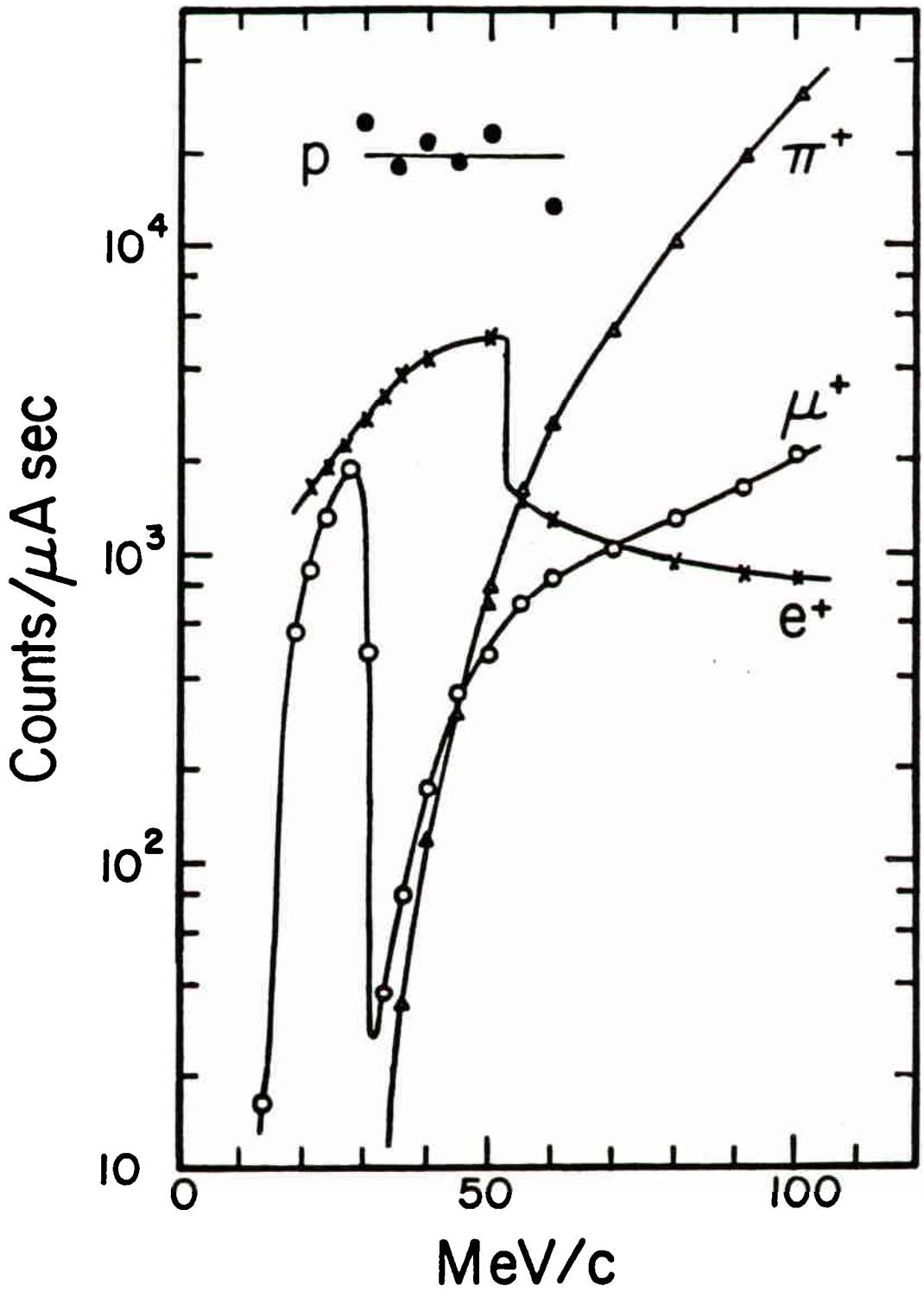

FIGURE (5.2). Particle fluxes versus beamline momentum setting (taken from ref. 46).

horizontally, and 5 mm and 70 mrad vertically.

Beam e^+ pass through the stopping target and do not satisfy the trigger requirements. Beam protons are stopped far upstream, mostly in the beamline vacuum window. The pulsed nature of the primary proton beam allows prompt π^+ and μ^+ from π^+ decay in flight to be eliminated by timing cuts relative to the cyclotron rf cycle.

Approximately 2% of the μ^+ flux originates from π^+ decay in flight. These 'cloud' μ^+ are, on average, far less polarized than the surface muons. As an extreme example, the (V-A) backward decay of an 81.0 MeV/c π^+ yields a forward moving 29.5 MeV/c μ^+ with parallel spin and momentum directions, thereby mimicking a (V+A)-produced surface muon. However, efficient transport of cloud muons to the stopping target beam spot (F3) requires the in-flight π^+ decays to occur close to the production target, i.e. to be prompt. The primary protons arrive at the production target in bursts of 2-5 nsec duration 43 nsec apart. In Figure (5.3)(a) the exponential decay of π^+ at rest (τ_π=23 nsec) underlies the time distribution, relative to the cyclotron rf cycle, of 29.5 MeV/c μ^+ arriving at the stopping target. The residual cloud μ^+ and prompt π^+ peaks are clearly visible in the Figure (5.3)(b) arrival times of 30.5 MeV/c beam particles. Events with beam particle arrival times in the shaded regions of Figure (5.3), which contain 98% of the cloud μ^+, are rejected in the data analysis.

5.2 The Apparatus: An Overview

After traversing the beamline the beam passed through a 2 mil mylar vacuum window and entered the apparatus shown in Figure (5.4). Beam μ^+ were stopped in either a metal foil or liquid helium target positioned

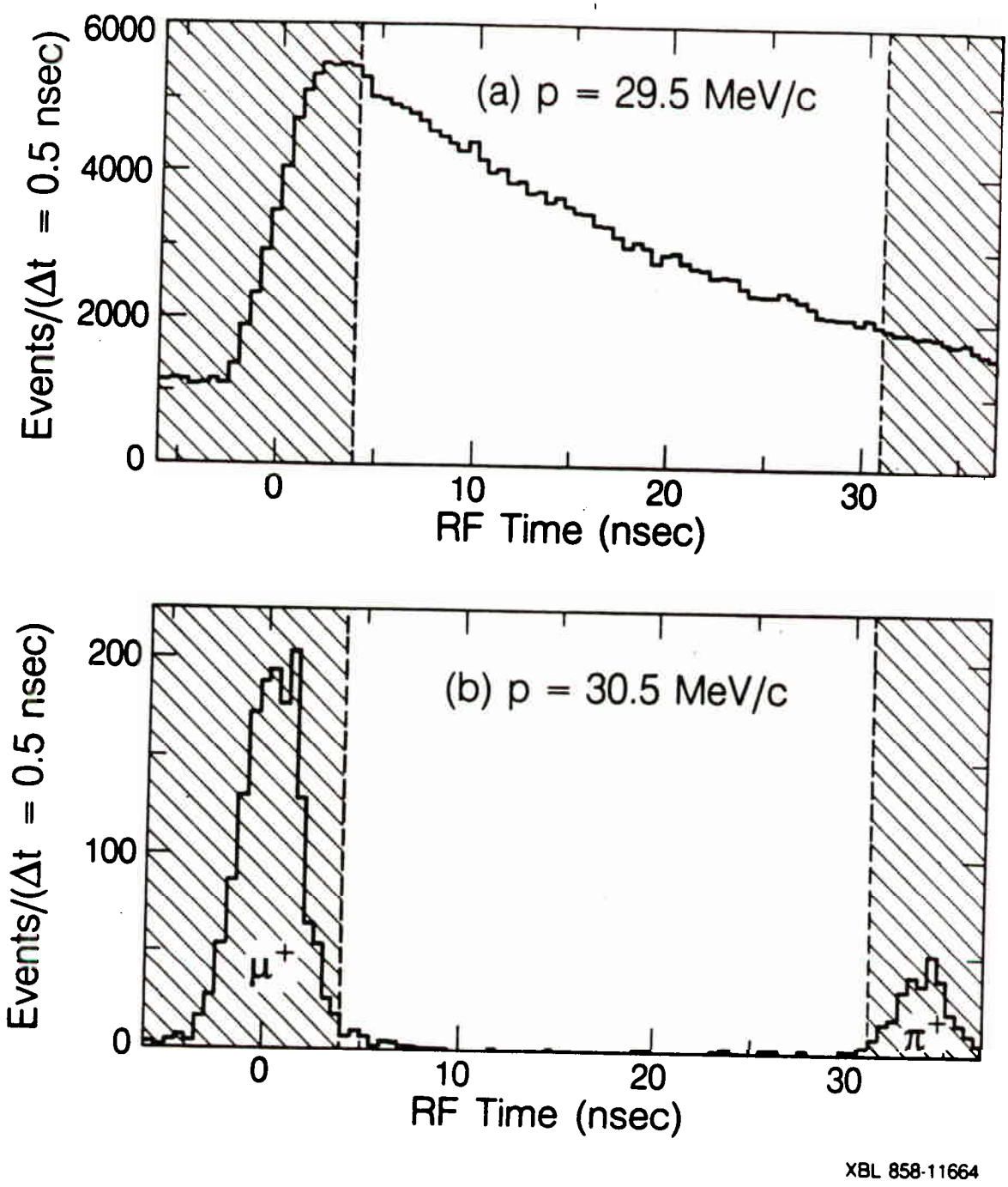

FIGURE (5.3). Beam particle arrival times with respect to the 43 ns cyclotron rf cycle at (a) 29.5 MeV/c and (b) 30.5 MeV/c. The shaded regions contain almost all of the cloud μ^+ and prompt π^+ contaminations and are rejected.

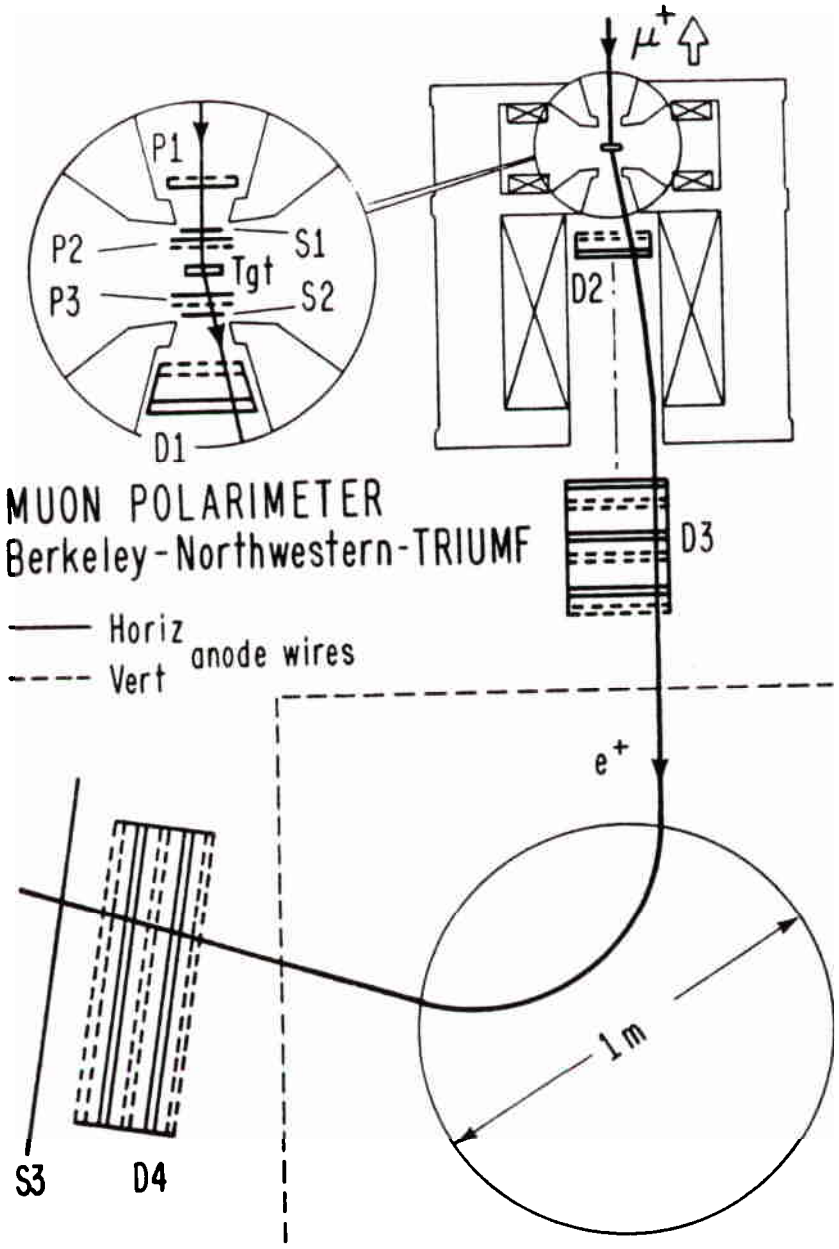

FIGURE (5.4). The apparatus. P1-P3 are proportional chambers; S1-S3 are scintillators; D1-D4 are drift chambers. Muons entering the solenoid are stopped in the target (Tgt). Decay e^+ emitted near the beam direction are focused by the solenoid into the spectrometer.

at the center of the upstream section of the solenoid. The amount of material upstream of the stopping target was estimated to be 50 mg/cm^2 in Run 1, 54 mg/cm^2 in Run 2, and 55 mg/cm^2 in Run 3.

Decay e^+ emitted within 270 mrad of the beam direction were focused by the downstream section of the solenoid into a horizontally focusing cylindrical dipole spectrometer for momentum analysis. Multiwire proportional chambers and drift chambers in the target region measured the incoming beam μ^+ and outgoing decay e^+ trajectories. Tracks recorded by drift chambers located near the conjugate foci of the spectrometer allowed reconstruction of the decay e^+ momentum. The amount of material downstream of the stopping target and upstream of the spectrometer was estimated to be 186 mg/cm^2 in Run 1, 193 mg/cm^2 in Run 2, and 216 mg/cm^2 in Run 3.

5.2.1 The Solenoid

The solenoid consists of two co-axial sections essentially decoupled by the intervening septum. The two water-cooled coils of the upstream section produce the longitudinal field for the spin-held mode of the experiment. They have inner diameter 6", outer diameter 10", length 2", 29 turns/coil, and a center-to-center separation of 7". The pole faces and coil separation were designed to minimize radial field components over the target region. Computer simulations using the program POISSON indicated that within a radius of 1" and within ±0.25" longitudinally of the nominal target position the field direction is axial to within 2 mrad.

The vertical transverse field used in the μSR mode was produced by

an additional water-cooled coil. The μSR coil consisted of a single turn of 0.125" × 0.5" copper having four horizontal sections transverse to the beam direction with centers 1.125" above and below the beam axis and 1.94" upstream and downstream of the nominal target position. Studies using the program POISSON indicated that within ±1" of the beam axis and within ±0.7" longitudinally of the target position the longitudinal field component did not exceed 1.0% of the transverse field. Field measurements made with the coil outside the solenoid indicated field strength uniformity of ±0.4% within 0.75" of the beam axis at the nominal target position. Transverse fields of 70-G and 110-G were obtained with coil currents of 475-A and 750-A, respectively.

A residual longitudinal field of about 40-G remaining at the target position after the upstream longitudinal field coils were turned off was nulled to within 2-G by applying a small reverse current to the coils. The null condition was indicated by a maximal ratio of events to stopped μ^+ in Run 1, and by field measurements in Runs 2 and 3.

The downstream section of the solenoid has three coils each with inner diameter 4.5", outer diameter 10", length 6.25" and 120 turns/coil.

Table (5.1) shows the on-axis longitudinal fields calculated by POISSON for the spin-held (B_L) and μSR (B_T) modes. The stopping target position is at zero, with downstream positions being positive. The field values assume 1.31×10^5 A-turns/coil downstream, and 5.45×10^4 A-turns/coil upstream for B_L. For $z>11.25"$ $B_{Lz}=B_{Tz}$.

z (inch)	$B_{Lz}(z)$ (Gauss)	$B_{Tz}(z)$ (Gauss)	z (inch)	$B_{Lz}(z)$ (Gauss)	$B_{Tz}(z)$ (Gauss)	z (inch)	$B_{Tz}(z)$ (Gauss)
-4.25	283		6.50	5439	5412	22.25	8828
-4.00	388		6.75	6034	6011	22.50	8730
-3.75	528		7.00	6569	6550	22.75	8600
-3.50	719		7.25	7081	7064	23.00	8454
-3.25	1028		7.50	7522	7507	23.25	8291
-3.00	1538		7.75	7894	7881	23.50	8110
-2.75	2385		8.00	8217	8205	23.75	7910
-2.50	3627		8.25	8491	8480	24.00	7691
-2.25	5429		8.50	8721	8711	24.25	7451
-2.00	7358		8.75	8913	8903	24.50	7191
-1.75	9035		9.00	9073	9064	24.75	6912
-1.50	10268		9.25	9204	9195	25.00	6611
-1.25	11014		9.50	9315	9307	25.25	6293
-0.75	11654		9.75	9406	9399	25.50	5956
-0.50	11754		10.00	9480	9473	25.75	5610
-0.25	11801		10.25	9533	9526	26.00	5256
0.00	11811	0	10.50	9580	9573	26.25	4895
0.25	11805	1	10.75	9617	9611	26.50	4527
0.50	11763	2	11.00	9648	9642	26.75	4168
0.75	11668	3	11.25	9674	9668	27.00	3821
1.00	11450	6	11.50		9690	27.25	3483
1.25	11038	11	12.00		9728	27.50	3159
1.50	10300	21	12.50		9755	27.75	2847
1.75	9079	34	13.00		9771	28.00	2559
2.00	7421	56	13.50		9788	28.25	2295
2.25	5523	89	14.00		9794	28.50	2048
2.50	3765	138	14.50		9794	28.75	1819
2.75	2587	206	15.00		9788	29.00	1613
3.00	1821	290	15.50		9782	29.25	1428
3.25	1406	387	16.00		9770	29.50	1260
3.50	1214	505	16.50		9758	29.75	1109
3.75	1170	654	17.00		9738	30.00	974
4.00	1208	831	17.50		9712	30.25	855
4.25	1323	1050	18.00		9676	30.50	749
4.50	1525	1321	18.50		9637	30.75	656
4.75	1803	1649	19.00		9588	31.00	572
5.00	2146	2030	19.50		9531	31.50	435
5.25	2564	2475	20.00		9458	32.00	333
5.50	3059	2990	20.50		9367	32.50	259
5.75	3596	3542	21.00		9251	33.00	220
6.00	4184	4142	21.50		9110	33.50	174
6.25	4805	4772	22.00		8932	34.00	139
						36.00	65

Table (5.1)

5.2.2 The Spectrometer

The spectrometer consisted of an NMR-monitored horizontally focusing cylindrical dipole magnet with drift chambers located near its conjugate foci. The magnet was originally used by Sagane et al.[47] in measurements of the muon decay ρ parameter. The flat pole faces have a diameter of 37" and were separated by a gap of 14.5". When operated at 125-A the water-cooled coils produced a central field of 0.32-T, a 98° bend angle for x=1 decay e^+, and a momentum dispersion of 1.07%/cm. Enclosing the particle trajectories by a vacuum box with 5 mil mylar vacuum windows positioned close to the conjugate focal planes minimized momentum resolution loss due to multiple Coulomb scattering. Drift chambers D3 and D4 [Figure (5.4)] were mounted to the vacuum box immediately upstream and downstream of the vacuum windows, repectively.

5.2.3 Proportional Chambers

The proportional chambers P1, P2, and P3 each had one horizontal and one vertical wire plane separated by a grounded 0.5 mil double-side aluminized mylar sheet. The anode wires were 0.5 mil diameter gold-plated tungsten with 2 mm spacing. Cathode signals obtained from the 0.5 mil single-side aluminized mylar chamber windows were used in the trigger.

Chamber P1 had circular aperture and 32 wires per plane. The windows and ground plane were 4 mm from the wire planes. Chambers P2 and P3 were of identical construction with square aperture and 30 wires per plane. The windows and ground plane were 2 mm from the wire planes.

In Runs 1 and 3 the proportional chamber gas was 92% methane/8%

methylal, and in Run 2 magic gas: 69.7% argon, 30.0% isobutane and 0.3% freon.

The operating voltages, applied to the wires, were 3500 V for P1 and 2500 V for P2 and P3 when using methane/methylal; and 2950 V for P1 and 2050 V for P2 and P3 when using magic gas. Amplifiers for the wire and cathode signals were positioned close to the chambers. The mean efficiency of the wire planes was >99.5% per plane.

An additional chamber, denoted 'A' and identical to P2 and P3, was positioned between P1 and P2 in Run 3 in preparation for a measurement of the decay parameter δ where the extended data momentum range (20-53 MeV/c) made highly efficient rejection of 'straight-through' beam e^+ events essential.

5.2.4 Drift Chambers

The planar drift chambers D1-D4 [Figure (5.4)] were composed of sub-units each containing two planes of horizontal or vertical sense wires. The sense planes were staggered by a half cell width to resolve left-right ambiguities. The cell geometries used in D1, D2 and D3, and D4 are shown in Figure (5.5). The sense wires were 0.5 mil diameter gold-plated tungsten and the field wires were 3 mil diameter berylium-copper.

D1 was of conical geometry. The wire spacing within each plane was 0.400" and the spacing between planes was 0.35". In downstream order the two vertical and two horizontal sense planes contained 3, 4, 4 and 5 wires. The chamber windows were 0.5 mil aluminum.

D2 was cylindrical with a 7" diameter aperture. Each wire plane

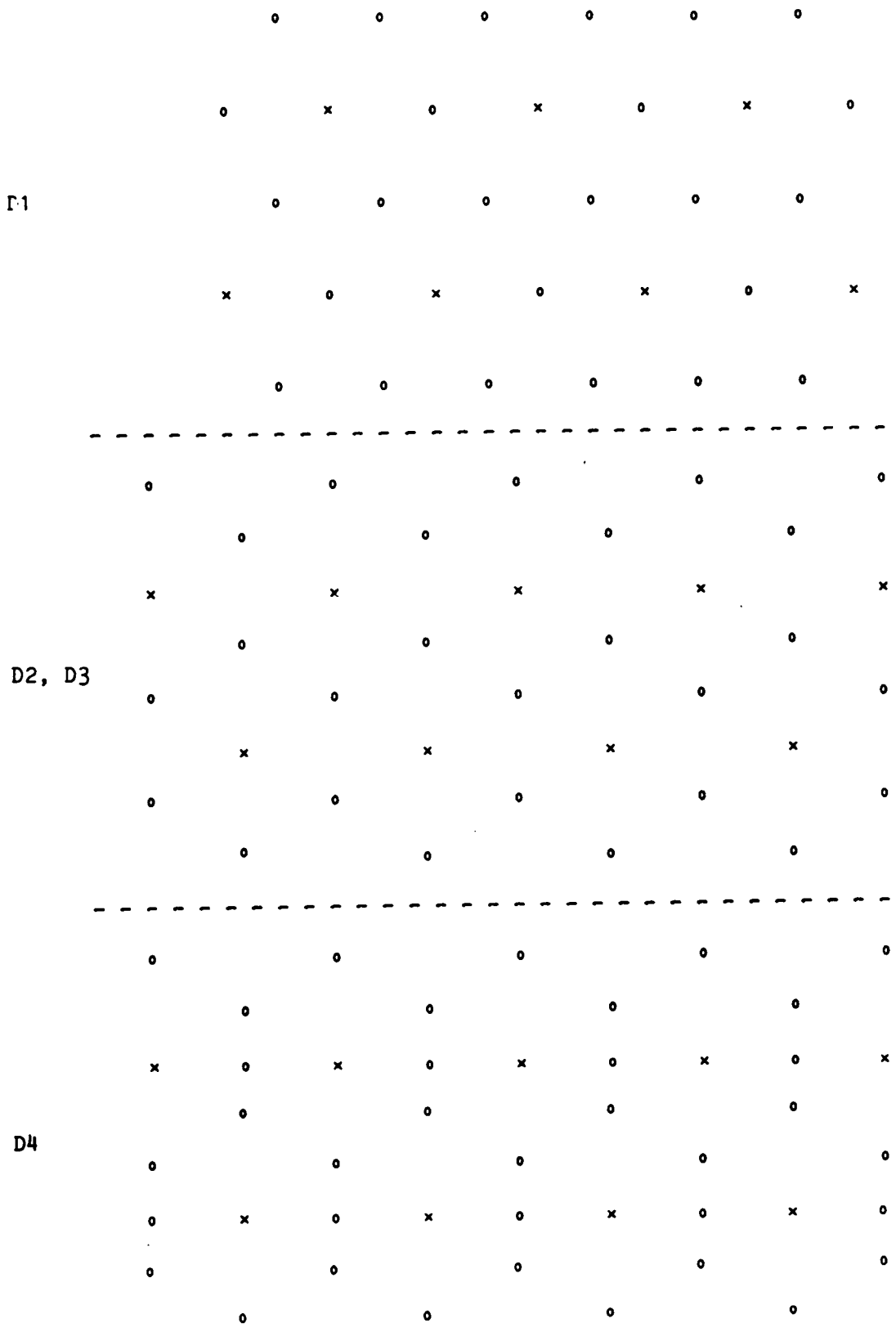

FIGURE (5.5). Drift-chamber cell geometries: × sense, ○ field.

contained 8 wires spaced by 0.875". The separation between planes was 0.250". The shortest, and potentially least efficient, edge wire in each sense plane was 3 mil berylium-copper to render it completely inactive. The chamber windows were 0.5 mil aluminized mylar.

D3, located at the spectrometer entrance, consisted of 3 cylindrical chambers similar to D2 except that the aperture diameter was 11" and there were 12 wires per plane. D3 thus had a total of 6 vertical and 6 horizontal sense planes. The three chambers were separated, except for a narrow outer annulus, by 0.25 mil aluminized mylar windows.

D4, located at the spectrometer exit, had a rectangular aperture and contained a total of 6 planes of 32 vertical sense wires and 4 planes of 24 horizontal sense wires. The sense wire spacing was 24 mm.

The drift chamber gas was 92% methane/8% methylal. The chamber high voltage was applied to the sense wires of D1, and to the field wires of D2, D3 and D4. The operating voltages were +2900 V for D1, -2900 V for D3, and -3000 V for D2 and D4. The efficiencies of the sense planes was equalized by applying +260 V to the sense planes closest to the chamber windows of D2, D3, and D4.

Chamber signals above a 250 μV threshold were amplified by shielded LeCroy Model 4292 amplifier/discriminator cards mounted close to the chambers. Each chamber had a mean efficiency of at least 97% per plane except in Run 1, where D1 and D2 had mean efficiencies of 77% and 83% per plane respectively.

5.2.5 Scintillators

Scintillators S1 and S2 were 5 mil and 10 mil NE102A, respectively. Just upstream of S1 and downstream of S2 were veto scintillators V1 and V2 each of thickness 0.125" and inner diameter 1.5".

Scintillator S3, which covered the downstream area of drift chamber D4 consisted of 3 horizontal strips 39" long × 8" high × 0.375" thick.

S1, S2, V1, V2 and each strip of S3 were viewed from left and right by photomultipliers.

5.2.6 Stopping Targets

The muons were stopped in metal foils of >99.99% purity or in liquid He. Because foils of optimum thickness were unavailable the stopping targets were composite, consisting either of two back-to-back foils or a single foil preceded and followed by 1 mil aluminum foils.

The stopping target thicknesses are tabulated in Table (5.2). The compositions of targets having 1 mil Al foils are listed in upstream to downstream order. The target material calculated to be encountered by decay e^+ emitted by a mean range μ^+ is listed as 'residual thickness.' The residual thickness is also tabulated in terms of calculated μ^+ rms range straggling lengths. The effect of the 1% $\Delta p/p$ momentum bite has been included. Column (a) gives the number of straggling lengths to the downstream surface of the target. Column (b) gives the number of straggling lengths to the closest interface between foils, the + (-) sign indicating that mean range μ^+ stop beyond (before) the interface. Comparison of the calculated ranges with an experimental range curve taken in Run 2 indicates that the error on the number of straggling

Target	Run	Thickness (mg/cm^2)	Residual Thickness (mg/cm^2)	Residual Straggling Lengths (a)	(b)
Ag	1	2× 136.5 Total 273	96	8.1	3.4^+
Al	1,2,3	150	35	4.6	3.7^-
Al*	2	2× 142.5 Total 285	171	22.6	3.6^+
Au	1,2	6× 6.6 Al 193 Au 6.6 Al Total 239	53 Au 6.6 Al Total 60	4.1	3.4^-
Cu	2	6× 6.6 Al 110 Cu 6.6 Al Total 156	16 Cu 6.6 Al Total 23	2.5	1.6^-
Cu*	1,2	2× 111 Total 222	81	8.3	3.1^+
He	1	38 Al 150 He 38 He Total 226	86 He 38 Al Total 124	17.2	

Table (5.2)

lengths is unlikely to exceed ±0.5. The Ag and He targets were used only in Run 1. The residual thicknesses and straggling lengths for the other targets apply to Run 2. The change of proportional chamber gas from methane/methylal to magic gas for Run 2 and the presence of an additional proportional chamber upstream of the target in Run 3 alter the residual thicknesses. In particular for the Al, Au and Cu* targets in Run 1 the number of residual straggling lengths in column (a) should be reduced by 0.5, and reduced (increased) in column (b) for a - (+)

sign. For Run 3 the number of residual straggling lengths for the Al target should be increased by 0.1 in both columns (a) and (b).

Muons stopping in the air between or beyond the foils, or in the foils' oxidized surface layers are likely to form muonium and depolarize. Column (b) indicates that the Cu target is too thin. The other targets most likely to have thickness problems are Cu* in Run 2 and Au in Run 1.

5.3 The Trigger

The essential features of the trigger logic as it existed in Run 1 are shown in Figure (5.6). Changes made to the logic in Runs 2 and 3 are described later in this section.

The inputs to the trigger logic were signals from the proportional chamber (P1-P3) cathodes, scintillators (S1-S3) and scintillator vetos (V1,V2) described in the preceding sections and shown in Figure (5.4). The notation P1U, P1V etc. denotes the cathodes associated with the wire planes measuring the horizontal and vertical track positions respectively. S1L and S1R etc. denotes photomultipliers viewing the scintillators from left and right repectively. The three horizontal scintillator strips of S3 were viewed from left and right, and in top to bottom order, by photomultipliers denoted by (G1,G4), (G2,G5), and (G3,G6).

Three triggers were used: the straight-through trigger for spectrometer momentum calibration with beam e^+; the μ-decay trigger for normal data taking; and the pulser trigger for online diagnostics such as checking ADC pedestals and searching for 'hot' or oscillating

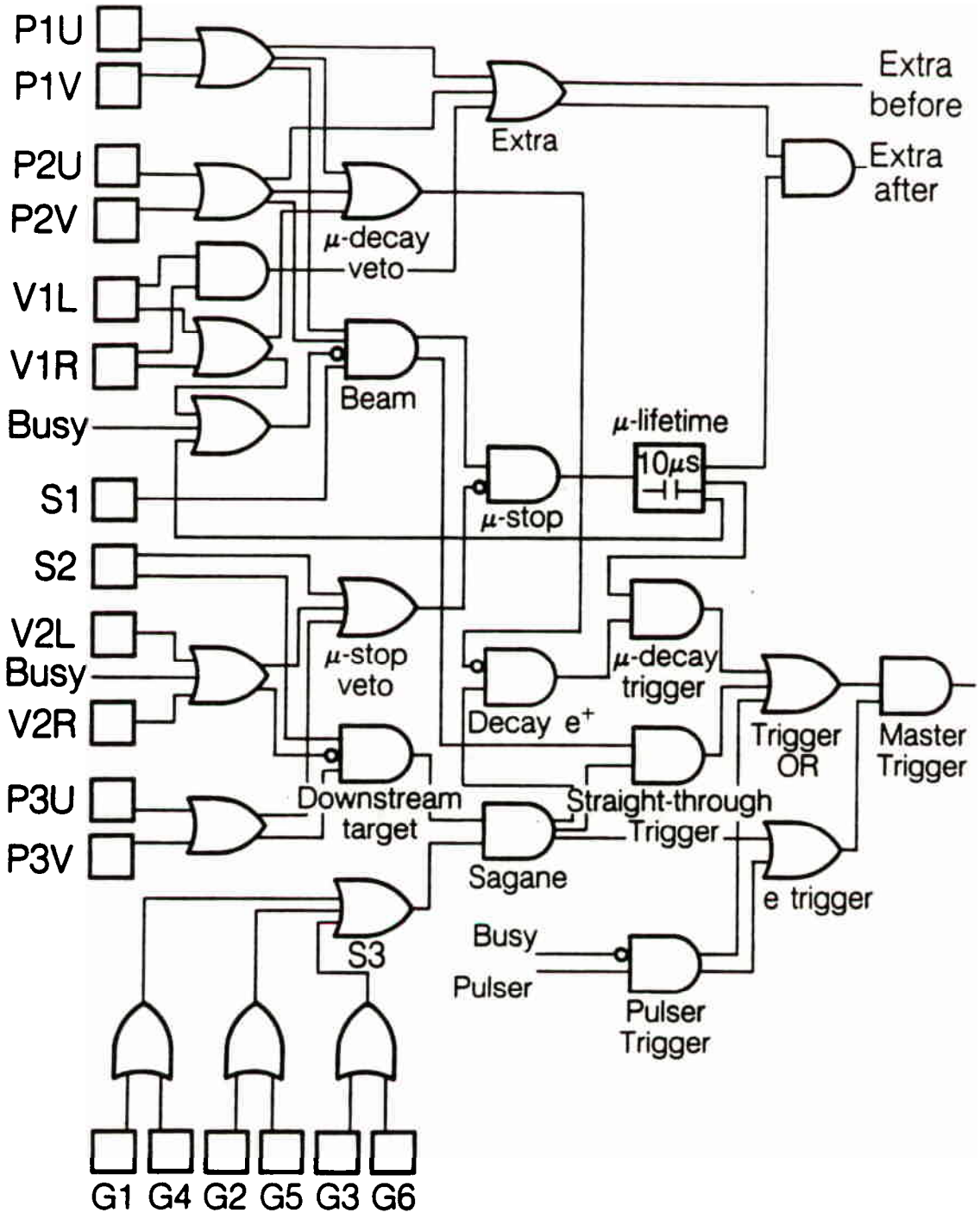

FIGURE (5.6). Essential features of the trigger logic during Run 1. Subsequent minor changes are described in the text.

wire-chamber channels.

Beam particles reaching the stopping target region have the signature

$$\text{Beam} = P1.P2.S1.\overline{V1}$$

Particles leaving the stopping target region and traversing the Sagane spectrometer have the signature

$$\text{Sagane} = P3.S2.S3.\overline{V2}$$

The straight—through trigger seeks to identify single beam particles which traverse the whole apparatus, and thus requires a coincidence between Beam and Sagane:

$$\text{Straight-through} = \text{Beam.Sagane}$$

The μ-decay trigger requires the signature of a μ-stop in delayed (0.1-10 μs) coincidence with that of a decay e^+. The μ-stop requirement that the beam particle stops in the stopping target is

$$\mu\text{-stop} = \text{Beam}.\overline{\mu\text{-stop veto}}$$

where $\overline{\mu\text{-stop veto}} = \overline{P3}.\overline{S2}.\overline{V2}$

The decay e^+ requirement that the outgoing downstream particle originates in the stopping target is

$$\text{Decay } e^+ = \text{Sagane}.\overline{\mu\text{-decay veto}}$$

where $\overline{\mu\text{-decay veto}} = \overline{P1}.\overline{P2}.\overline{V1}$

In Runs 2 and 3 P1 and P2 were removed from μ-decay veto and were replaced by the ability to make software cuts on events with P1 or P2

signals near the μ-decay time. The μ-stop time was provided by S1 and the μ-decay time by S2.

An important feature of the logic is the ability to tag, and later reject in software, almost all events where the decay e^+ could have originated from extra μ^+ rather than the μ-stop muon. This is crucial in the μSR mode of the experiment since extra μ^+ arriving at random times have correspondingly random precessed spin directions with respect to those of the μ-stop muons. They are therefore equivalent to an admixture of unpolarized muons and thus mimic right-handed current effects. The arrival of each beam particle sets a 10 μs latch. If a μ-stop occurs within the 10 μs latch the event is tagged as an 'extra-before'. In addition the arrival times of 'extra-after' beam particles arriving in the 10 μs following the μ-stop were recorded. A high incidence of false extra-after signals due to P1 and P2 after-pulsing following the μ-stop were largely eliminated by inserting dead-time notches in 'extra-after'. The resulting 'extra-after-1' and 'extra-after-2' were active from 0.6-10 μs and 0.85-10 μs in Run 1, and from 0.3-10 μs and 0.5-10 μs in Runs 2 and 3 respectively. The 1/4 OR of P1 and P2 cathode signals in Extra was replaced in Run 2 by either a 2/4 or a 3/4 coincidence, the choice depending on the proportional chamber cathode efficiencies. In Run 3 the role of P1 and P2 in Extra was assumed instead by the additional proportional chamber A between P1 and P2.

5.4 Data Acquisition

Event data was read from the CAMAC electronics into a circular buffer of a PDP-11/34 computer using the data acquisition program DA. The data was written to tape after several events were accumulated in the buffer. The program DA also supplied event information to the online analysis program MULTI.

Drift chamber time information was obtained using a LeCroy System 4290. The TDCs were operated in the common-stop mode, with the stop being provided by the trigger. Digitized time information was transferred to the memory unit which then sent a LAM signal to the PDP-11/34. In addition the PDP-11/34 read TDC and ADC information from the proportional chambers and scintillators; TDC information on the μ^+ arrival time relative to the cyclotron rf cycle, μ^+ lifetime, and extra-after times; latches set by proportional chamber wire signals and trigger logic elements; event scalers; and NMR-monitored fields in the beamline dipoles and spectrometer.

The CAMAC electronics were gated-off for 5 ms (reduced to 200 μs during Run 2) while the PDP-11/34 read the event and cleared the CAMAC electronics. In addition a computer 'busy' signal gated-off the trigger logic to prevent another trigger being received until the CAMAC electronics were cleared. It should be noted however that the extra-before latch remained operational during computer 'busy'.

Online information provided by MULTI included histograms of wire-chamber plane illuminations and multiplicities, the beam spot and angular distributions, the event time spectrum, scintillator and proportional chamber TDC and ADC distributions, and the proportion of events with extra-before and extra-after beam particles.

Typical event rates with 100 μA of protons incident on the production target were 60-70 Hz in the μSR mode and 25-30 Hz in the spin-held mode. The μSR data presented here were obtained from 1.5×10^7 raw triggers. The cuts described in Chapter 6 retained 5.6% of the events.

Chapter 6

Event Reconstruction

6.1 Wire Chamber Alignment

The relative positions of the wire chamber planes transverse to the beam direction were determined from the mean residuals of reconstructed beam e^+ tracks. Straight track segments were fitted to hits in the horizontal and vertical wire planes of the chamber groups P1, P2, P3, D1 and D2; D3; and D4 [Figure (5.4)] with the solenoid off and no stopping target between P2 and P3. Alignment of wire-chambers P1-D2 as a single unit ensured that the μ^+ and e^+ polar angles θ_μ and θ_e were measured relative to a common axis. The chamber planes were thereby aligned to within 50 μm, while the rms residuals were typically 300 μm in the drift chambers.

6.2 Muon Track Reconstruction

Straight muon tracks were fitted to hits in proportional chambers P1 and P2. A valid hit was defined to be a signal from at least one, but no more than three, adjacent wires in the same plane. The track was assumed to pass through the center of the hit pattern. One and only one hit was permitted in each plane of P1. One plane of P2 was also required to have one and only one hit, while either one or two hits were allowed in the other plane. The correct muon track was assumed to be the one agreeing most closely with the outgoing positron track in stopping target position. Events with reconstructed $\cos\theta_\mu<0.99$ with respect to the beam direction were rejected in the analysis.

6.3 Positron Track Reconstruction

Straight e^+ track segments were fitted separately to hits in the horizontal and vertical projections of the wire-chamber plane groups: P3, D1, D2; D3; and D4. Resolution of the left-right ambiguity associated with each drift chamber hit relied on the staggered cells of adjacent sense planes. The first sought track segments of acceptable straightness and slope were those with a hit in each of the constituent wire-chamber sense planes. In segments where such tracks were not found the number of sense planes required to have a hit on the track was progressively decreased. If more than one track was found with hits in the same number of planes the track with the best chi-square was accepted. Tracks in all six segments were found in 99% of the triggers.

To guard against fake tracks from spurious hits, cuts were made on the total number of hits in the wire chamber groups. The number of hits in the 10 planes of P3-D2 and in the 10 planes of D4 were each required to be ≤ 18; and in the 12 planes of D3 to be ≤ 22. Furthermore, the horizontal and vertical track projections in P3-D2 were each required to have hits in at least 3 of the 5 constituent planes; in D3 to have hits in at least 4 of the 6 planes horizontally and 3 of the 6 planes vertically; and in D4 to have hits in at least 4 of the 6 planes horizontally and 3 of the 4 planes vertically. In addition only one hit, as defined in section (6.2), was permitted in each plane of P3.

The e^+ tracks through P3-D2 are not straight because of the longitudinal field in the downstream section of the solenoid. The P3-D2 track space points were refitted to a curved track based on the first-order optics of cylindrically symmetric fields described in Appendix A. The best fit tracks were obtained using field values 95% of

those in Table (5.1).

Approximate space:time relations were obtained by integrating the drift-time distributions of cells almost uniformly illuminated by decay e^+ in μSR runs with the downstream solenoid off. The e^+ curved track residuals were used to dynamically fine-tune the space:time relation for each drift chamber plane in each run. The space:time relations for the various planes were stored as arrays of drift distances for each of 512 1-nsec wide drift-time bins. The first 3000 events on each data tape, typically containing 1.2×10^5 events, were used for the fine-tuning after which the tape was rewound and the analysis restarted. If for the i'th drift-time bin a residual r was obtained, the drift distances for the i-8 to i+8 time bins were changed by

$$\Delta(i\pm k) = (\text{sign})rW[9-\max(k,1)]/200$$

for $0 \le i\pm k \le 512$ where $0 \le k \le 8$,

$$W = \begin{cases} 1.0 \text{ if } |r| < 0.1 \text{ cm} \\ 0.5 \text{ if } 0.1 \text{ cm} < |r| < 0.2 \text{ cm} \\ 0 \text{ if } |r| > 0.2 \text{ cm} \end{cases}$$

and

$$\text{sign} = \begin{cases} +1 \text{ if track coordinate} > \text{wire coordinate} \\ -1 \text{ if track coordinate} < \text{wire coordinate} \end{cases}$$

The changes are therefore largest for the i'th and i±1'th drift-time bins and then decrease linearly away from the i'th bin. The procedure converges after about 1500 events.

The drift-chamber rms residuals are shown in Table (6.1). The larger rms residual in the D1 vertical projection is not well understood. The 3% of events with e^+ tracks in P3-D2 with reduced $\chi^2>20$ were rejected.

Drift Chamber	RMS Residual (μm)
D1 (horizontal)	325
(vertical)	600
D2	325
D3	250
D4	250

Table (6.1)

The e^+ track segments fitted in P3-D2; D3; and D4 were required to satisfy several continuity criteria. First-order optics (Appendix A) extrapolations of the tracks in P3-D2 and D3 into the solenoid bore were required to have both radial agreement, ΔR, and azimuthal agreement, $R\Delta\phi$, <2 cm. Extrapolations of the tracks in D3 and D4 into the spectrometer were required to agree to within 4 cm in both vertical position and impact parameter with respect to the magnet axis, and to agree to within 0.08 in vertical slope. The horizontal position of the e^+ track determined by the S3 scintillator pair time difference was required to agree with the extrapolated D4 track to within 10 cm. Events in which more than one of the three S3 scintillator pairs fired were rejected.

Aperture cuts were made in the solenoid and spectrometer. Events with e^+ emitted from the stopping target at radii >1.8 cm or with $\cos\theta_e<0.975$ were rejected. The e^+ track radial position at the exit of D2 (aperture radius 8.86 cm) was required to be <8.5 cm. The maximum track radial position in the solenoid bore (aperture radius 11.1 cm)

was required to be <10 cm. The presence of gas lines (Runs 2 and 3) and a helium bag (Run 2) in addition to D2 signal cables within the solenoid bore made necessary tighter radial cuts of 8.5 cm in Run 2 and 9.5 cm in Run 3. The vertical position of the track at the spectrometer exit (vertical aperture ±16.8 cm) was required to be within ±15.5 cm of the median plane. Additional vertical cuts were made at ±(6.4-9.4) cm around two horizontal ribs supporting the vacuum window between the spectrometer and D4.

6.4 Extra Muons

Most e^+ originating not from the decay of the observed stopped μ^+, but from the decay of another μ^+ were eliminated by rejecting events with 'extra-before' or 'extra-after-1' [section (5.3)] beam particles. The small fraction of events with e^+ originating from untagged extra μ^+ was reduced by requiring continuity between the e^+ and μ^+ tracks at the stopping target. Requiring track separations <4.5 mm rejected 78% of uncorrelated μ^+-e^+ events and 14% of correlated μ^+-e^+ events.

Positrons from extra μ^+ with random arrival times constitute a flat background to the observed μ^+ decay time spectrum. A comparison of the background levels before and after the cuts described above therefore provides a measure of the efficiency of those cuts. Figure (4.1) shows the Run 2 spin-held data time spectrum after the cuts were made. The fitted background of 1.3±9.8 per time bin corresponds to $(3\pm22)\times10^{-5}$ of the time t=0 rate. Before making the cuts a spectrum with a similar number of events at early times had a background of about 1600 per time bin, or 3.6×10^{-2} of the t=0 rate.

6.5 Momentum Reconstruction

The momenta of e^+ passing through the horizontally focusing cylindrical dipole spectrometer were obtained to first order from the sum of the horizontal coordinates at the conjugate foci. A nominal x=1 calibration point was provided by the sharp edge at the endpoint of the μSR data. The spectrometer momentum dispersion was measured to be approximately 1.07%/cm using e^+ beams obtained at several settings of the beamline elements.

Empirical ad hoc corrections were introduced to make the reconstructed μSR data endpoint independent of impact parameter with respect to the magnet axis, mean squared (vertical) deviation from the median plane, and vertical position at the spectrometer exit. This procedure was repeated at several spectrometer settings to obtain corrections appropriate for x=1 at the standard spectrometer setting. An additional correction eliminated a residual correlation between $\cos\theta_e$ and the reconstructed endpoint, which amounted to $\Delta x=0.001$ between the $\cos\theta_e=0.975$ and $\cos\theta_e=1$ endpoints. The resulting momentum resolution was better than 0.2% rms.

The spectrometer was re-calibrated with e^+ beams obtained at many beamline settings. In Run 3 two sets of calibration data were taken with the spectrometer at 42%, 50%, 60%, 72%, 86%, and 100% of its standard setting, while in Runs 1 and 2 only the standard setting was used. After allowing for a most probable e^+ energy loss of 1.75 MeV-cm^2/g in the material upstream of the spectrometer, the e^+ momentum was assumed to be proportional to the beamline dipole settings. Any apparent non-linearities or offsets were attributed to the spectrometer. With the coefficients of the linear and quadratic

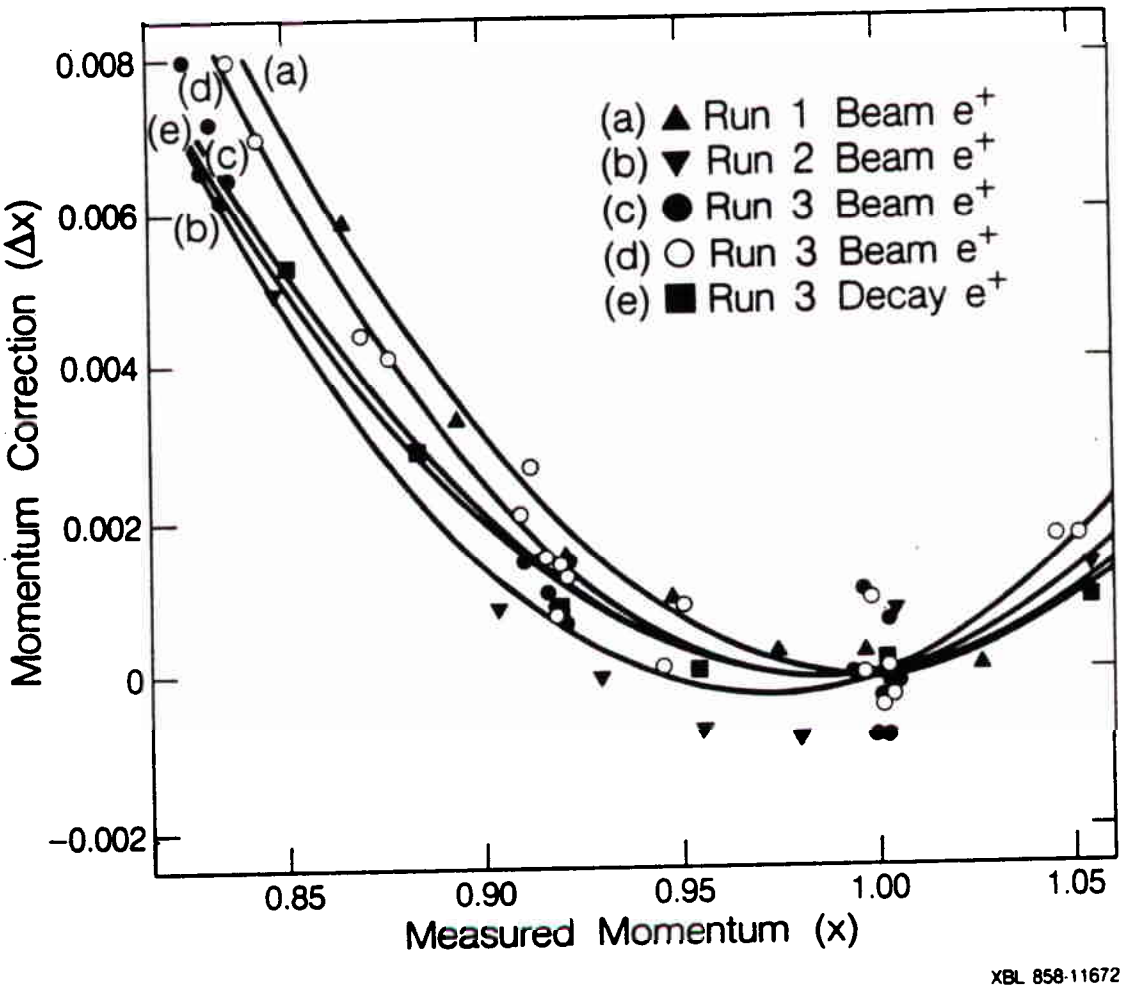

FIGURE (6.1). Momentum correction versus nominal measured momentum required to yield linear momentum scale with x=1 unchanged. The curves are quadratic fits to the points. Additional points with x>1.05 in calibrations (c)-(e) were included when determining curves (c)-(e).

dispersion terms allowed to vary linearly with spectrometer setting it was found that:

(i) the effective field integral for particles with a 98° bend angle at the various spectrometer settings increased (0.22±0.02)% more rapidly than indicated by the NMR probe in the central field region;

(ii) the linear dispersion increased by (1.1±0.2)% between the spectrometer 42% and 100% settings;

(iii) the quadratic dispersion was consistent with being constant.

An independent calibration, incorporating the above spectrometer behavior, was performed using the reconstructed μSR data endpoints at several spectrometer settings. The result was consistent with the beamline calibrations, thereby indicating that the beamline did not deviate appreciably from the assumed linear behavior.

The calibration data displayed in Figure (6.1) shows the correction required at the standard spectrometer setting to convert the original momentum scale to a linear momentum scale leaving the nominal x=1 point unchanged. The mean of the five curves in Figure (6.1) was taken to be the required momentum correction.

Conversion of the linear momentum scale to an absolute momentum scale is illustrated by the following exmaple. The endpoint of the Run 3 Al target data was at x=1.0030 on the linear momentum scale. Allowing for uniform energy-loss in the material upstream of the spectrometer the expected endpoint is at x=0.9916 on the absolute momentum scale. Thus a factor of 0.9886 converts the linear momentum scale to the absolute scale. For data fitting, uniform energy-loss was added back on to superimpose the data on the energy-loss straggled theoretical spectra (Appendix B). Since the calibration beam e^+ and the decay e^+

traverse similar amounts of material, the likely error in estimating the uniform energy-loss has negligible effect on the momentum ultimately attributed to the decay e^+.

The 1σ possible systematic error in the momentum calibration was taken to be the standard deviation of the corrections given by the five curves in Figure (6.1). They are shown in Table (6.2) for the centers of the momentum bins used in the data analysis.

Momentum x	Standard Deviation in Correction Δx
0.89	0.00066
0.91	0.00053
0.93	0.00040
0.95	0.00029
0.97	0.00017
0.99	0.00006

Table (6.2)

The above momentum calibration systematic errors are to be added in quadrature with a likely error of ± 0.0001 in determining the μSR data endpoint.

Events with $x<0.88$ ($x<0.92$ in Run 1), which have lower statistical power and larger possible systematic errors in momentum reconstruction, were rejected in the analysis.